

The ALMA Frontier Fields Survey

IV: Lensing-corrected 1.1 mm number counts in Abell 2744, MACSJ0416.1-2403 and MACSJ1149.5+2223

A. M. Muñoz Arancibia¹, J. González-López², E. Ibar¹, F. E. Bauer^{2,3,4}, M. Carrasco⁵, N. Laporte⁶, T. Anguita^{7,3}, M. Aravena⁸, F. Barrientos², R. J. Bouwens⁹, R. Demarco¹⁰, L. Infante^{2,11}, R. Kneissl^{12,13}, N. Nagar¹⁰, N. Padilla², C. Romero-Cañizales^{3,8}, P. Troncoso¹⁴, and A. Zitrin¹⁵

¹ Instituto de Física y Astronomía, Universidad de Valparaíso, Av. Gran Bretaña 1111, Valparaíso, Chile
e-mail: alejandra.munozar@uv.cl

² Instituto de Astrofísica y Centro de Astroingeniería, Facultad de Física, Pontificia Universidad Católica de Chile, Casilla 306, Santiago 22, Chile

³ Millennium Institute of Astrophysics, Chile

⁴ Space Science Institute, 4750 Walnut Street, Suite 205, Boulder, CO 80301, USA

⁵ Zentrum für Astronomie, Institut für Theoretische Astrophysik, Philosophenweg 12, 69120 Heidelberg, Germany

⁶ Department of Physics and Astronomy, University College London, Gower Street, London WC1E 6BT, UK

⁷ Departamento de Ciencias Físicas, Universidad Andres Bello, Av. República 252, Santiago, Chile

⁸ Núcleo de Astronomía de la Facultad de Ingeniería y Ciencias, Universidad Diego Portales, Av. Ejército 441, Santiago, Chile

⁹ Leiden Observatory, Leiden University, 2300 RA Leiden, The Netherlands

¹⁰ Department of Astronomy, Universidad de Concepción, Casilla 160-C, Concepción, Chile

¹¹ Carnegie Institution for Science, Las Campanas Observatory, Casilla 601, Colina El Pino S/N, La Serena, Chile

¹² Joint ALMA Observatory, Alonso de Córdova 3107, Vitacura, Santiago, Chile

¹³ European Southern Observatory, Alonso de Córdova 3107, Vitacura, Casilla 19001, Santiago, Chile

¹⁴ Universidad Autónoma de Chile, Av. Pedro de Valdivia 425, Santiago, Chile

¹⁵ Physics Department, Ben-Gurion University of the Negev, P.O. Box 653, Be'er-Sheva 8410501, Israel

ABSTRACT

Context. Characterizing the number counts of faint (i.e. at the sub-mJy level and below), dusty star-forming galaxies is currently a challenge even for deep, high-resolution observations in the FIR-to-mm regime. They are predicted to account for approximately half of the total extragalactic background light at those wavelengths. Searching for dusty star-forming galaxies behind massive galaxy clusters benefits from strong lensing, enhancing their measured emission while increasing spatial resolution. Derived number counts depend, however, on mass reconstruction models that properly constrain these clusters.

Aims. We estimate the 1.1 mm number counts along the line of sight of three galaxy clusters, i.e. Abell 2744, MACSJ0416.1-2403 and MACSJ1149.5+2223, which are part of the ALMA Frontier Fields Survey. We aim to correct these counts by lensing effects, probing the sub-mJy flux density level and below.

Methods. We create a source catalog based on ALMA 1.1 mm continuum detections. We correct for magnification their observed flux densities using several, publicly available lensing models for these clusters. We perform Monte Carlo simulations of the number counts for a detailed treatment of the uncertainties in the magnifications and adopted source redshifts.

Results. We estimate lensing-corrected number counts at 1.1 mm using source detections down to S/N = 4.5. In each cluster field, we find an overall agreement among the number counts derived for the different lens models, despite their systematic variations regarding source magnifications and effective areas. Combining all cluster fields, our number counts span ~ 2.5 dex in demagnified flux density, from several mJy down to tens of μ Jy. Down to ≈ 0.1 mJy, both our differential and cumulative number counts are consistent with recent estimates from deep ALMA observations. At fainter flux densities, however, they are lower by ≈ 0.5 and ≈ 1 dex respectively, suggesting a flattening in the number counts.

Conclusions. We derive 1.1 mm number counts around three well-studied galaxy clusters down to ≈ 4 times deeper than the rms level reached in their ALMA mosaics. This highlights the potential of finding fainter sources in these cluster fields with deeper ALMA observations.

Key words. gravitational lensing: strong - galaxies: high-redshift - submillimeter: galaxies

1. Introduction

Observations at far-infrared (FIR) to millimeter (mm) wavelengths have revealed a population of dusty star-forming galaxies (DSFGs, see Casey et al. 2014 and references therein). The detection of these sources benefits from the negative k -correction in their spectral energy distribution (SED), which keeps their

measured flux density in the FIR-to-mm roughly constant up to redshift $z \approx 6 - 10$ (Blain et al. 2002). Bright sources were first detected using single-dish telescopes (e.g. Smail et al. 1997; Hughes et al. 1998). After exhaustive identification efforts and spectroscopic campaigns, they were found to lie at high redshift

with a peak at $z \sim 2 - 2.5$ (e.g., Chapman et al. 2005; Greve et al. 2005; Pope et al. 2006; Younger et al. 2007).

The surface density of DSFGs detected at different wavelengths is quantified through galaxy number counts (e.g. Blain et al. 1999). The bright end of the galaxy distribution has been extensively probed with single-dish telescopes (e.g. Coppin et al. 2006; Weiß et al. 2009). Recent interferometric follow-up observations of bright sources (≥ 5 mJy at $870\mu\text{m}$) have resolved some of them into multiple components (Smolčić et al. 2012; Karim et al. 2013; Hodge et al. 2013). Fainter DSFGs comprise the bulk of the star formation activity at high redshifts. It has been estimated that sources having $\approx 0.1 - 1$ mJy at 1.2 mm account for $\geq 50\%$ of the total extragalactic background light (EBL) at mm wavelengths (e.g. Ono et al. 2014; Carniani et al. 2015; Aravena et al. 2016; Fujimoto et al. 2016; Hatsukade et al. 2016; Hsu et al. 2016; Oteo et al. 2016). Better constraints await a complete census of fainter galaxies at these wavelengths in order to fully understand the various contributions to the EBL. Importantly, measuring the source brightness at several FIR-to-mm bands helps to disentangle how the rest-frame FIR spectra vary among galaxy populations; this serves as a key constraint for models of galaxy formation and evolution (see Safarzadeh et al. 2016 and references therein).

Faint flux densities can be probed in two ways, i.e. 1) performing deeper, high-resolution observations (compared to current confusion-limited single-dish data), or 2) using strong gravitational lensing by massive galaxy clusters (Hezaveh & Holder 2011). The high sensitivity of the Atacama Large Millimeter/submillimeter Array (ALMA) recently allowed the possibility to probe and characterize the faint end of the unlensed sub-mm population (Ono et al. 2014; Carniani et al. 2015; Oteo et al. 2016; Hatsukade et al. 2016; Aravena et al. 2016; Dunlop et al. 2017). On the other hand, the lensing power enhances the measured flux density of background sources and alleviates the effects of confusion (Blain et al. 1999). Some of the very first single-dish detections were done in galaxy cluster fields (Smail et al. 1997). Number counts from single-dish detected sources behind galaxy clusters have successfully probed flux densities down to the sub-mJy level albeit with a statistical approach, since counterparts are not firmly known (e.g., Knudsen et al. 2008; Zemcov et al. 2010; Johansson et al. 2011; Hsu et al. 2016). Combining both approaches can maximize their benefits. For instance, Fujimoto et al. (2016) derived 1.2 mm number counts down to a flux density of ~ 0.02 mJy (3σ), using proprietary and archival deep ALMA data that included 66 blank fields and one lensed galaxy cluster field.

In this work, we derive 1.1 mm number counts using dedicated ALMA observations (González-López et al. 2017, hereafter Paper I) and recent publicly available lensing models. We exploit ALMA’s unique capabilities to search for sources behind three well-studied galaxy clusters, which are part of the Frontier Fields survey (FFs, Lotz et al. 2017). This is a legacy project combining the power of gravitational lensing of massive clusters with extremely deep multi-band HST and Spitzer imaging of six strong-lensing clusters and adjacent parallel fields. With the help of several detailed mass models for each galaxy cluster, we can harness the magnification power of these clusters to recover the intrinsic (i.e., “delensed”) emission from background galaxies. In turn this may allow us to probe fainter flux densities when compared to observations from blank field surveys. Combining several cluster fields also helps to reduce the impact of cosmic variance, i.e., the field-to-field variation found in the volume density of sources due to large scale structure (Trenti & Stiavelli 2008).

This paper is organized as follows. §2 briefly describes the observational 1.1 mm data and public lensing models used in this work. §3 details the methodology used to derive the number counts, including a careful treatment of the uncertainties in magnification for a given lens model, source position and adopted redshift. §4 presents our derived demagnified 1.1 mm counts and places them in context compared to recent estimates from deep ALMA observations. §5 summarizes our main findings. Throughout this paper, we adopt a flat Λ CDM cosmology with parameters $H_0 = 70 \text{ km s}^{-1} \text{ Mpc}^{-1}$, $\Omega_m = 0.3$ and $\Omega_\Lambda = 0.7$, in order to match the cosmology for which the lens models were produced.

2. Data

2.1. Observations with ALMA

2.1.1. High-significance detections

The sources used in this work are drawn from the individual ALMA 1.1 mm detections in three of the galaxy clusters that comprise the FF survey, namely Abell 2744 ($z = 0.308$), MACSJ0416.1-2403 ($z = 0.396$) and MACSJ1149.5+2223 ($z = 0.543$), hereafter A2744, MACSJ0416 and MACSJ1149, respectively. They were observed as part of the ALMA Frontier Fields Survey (cycle 2 project #2013.1.00999.S, PI: F. Bauer). Paper I introduces the 1.1 mm mosaic images, data reduction and analysis for these galaxy clusters. Each field covers an observed area of $\sim 4.6 \text{ arcmin}^2$, and thus sum to a total image-plane area of $\sim 14 \text{ arcmin}^2$. This represents the largest area with high quality multi-wavelength coverage observed with ALMA to date, corresponding to ~ 3 times the area of the Hubble Ultra Deep Field (HUDF, Dunlop et al. 2017) and ~ 14 times the initial ALMA Spectroscopic Survey in the HUDF (ASPECS, Walter et al. 2016; Aravena et al. 2016). With natural weighting, our continuum data reach rms depths of $\sim 55 - 71 \mu\text{Jy beam}^{-1}$ and have synthesized beam sizes between $\sim 0''.5 - 1''.5$. A2744 was partially observed in a more extended configuration compared to the other cluster fields, leading to a longer mean projected baseline and better uv coverage of small structures. As a result, A2744 achieves the highest resolution among these fields (see Paper I for details).

For each cluster field, we take into account the primary beam (PB) correction. The source extraction is done within the region where $\text{PB} > 0.5$, i.e. where the PB sensitivity is at least 50% of the peak sensitivity. Sources are detected by searching for pixels with signal-to-noise ratio (S/N) ≥ 5 , which are then grouped as individual sources using the DBSCAN python algorithm (Pedregosa et al. 2012). In the following, we refer to the source S/N as the ratio of the peak intensity and the background rms. Note that depending on the spatial PB correction, sources having the same S/N may have different PB-corrected peak intensities. Unless noted, in the following we refer to source flux densities and peak intensities using PB-corrected values.

At $S/N \geq 5$, we detect seven sources in A2744, four in MACSJ0416 and one in MACSJ1149. Since some sources appear to be resolved, we measure their integrated flux densities performing two-dimensional elliptical Gaussian fits in the uv -plane using the UVMCMCFIT python algorithm (Bussmann et al. 2016). These fits also deliver the centroid position for each source. Before applying lensing corrections, detected sources have peak intensities in the range $\sim 0.33 - 1.43 \text{ mJy beam}^{-1}$ and integrated flux densities in the range $\sim 0.41 - 2.82 \text{ mJy}$. All of these sources have near-infrared (NIR) detected counterparts

(based on deep HST F160W imaging). None of them are members of a FF cluster. We refer the reader to Paper I for more details regarding the source extraction procedure, the choice of the uv -plane for estimating integrated source flux densities, and the search for NIR counterparts.

2.1.2. Going to fainter flux densities: $4.5 \leq S/N < 5$

We push below the $S/N \geq 5$ threshold of the 12 detections already reported in Paper I in order to extract more information from the maps contributing to the number counts. Although the probability of a spurious detection increases for all fields as we move to lower S/N values, we can statistically correct the counts for this effect. We decide to include all sources having $S/N \geq 4.5$ in the natural-weighted mosaics (see §3.2 for details), being extracted through the same procedure as high-significance detections. This adds four sources to A2744, one to MACSJ0416 and two to MACSJ1149.

Table 1 lists these detections, together with the high-significance detections from Paper I. Peak intensities of $4.5 \leq S/N < 5$ sources range from ~ 0.25 to ~ 0.52 mJy beam $^{-1}$. Since a two-dimensional Gaussian fit gives a highly uncertain measure of the integrated source flux density at low S/N ratios, we follow Fujimoto et al. (2016) and adopt the peak intensity of the detection as the best estimate of the integrated flux density, as size effects may influence the number counts only for highly lensed sources. Our assumption of point sources at low significance is supported by recent results regarding DSFG sizes, both from several publicly available ALMA maps at 1 mm (Fujimoto et al. 2017) and an ALMA follow-up of SCUBA2 sources in the CDFS at 850 μ m (González-López et al. 2018, in prep.). Fujimoto et al. (2017) find a positive correlation between source size and bolometric luminosity in the FIR; an extrapolation of this trend to lower luminosities may suggest that our sources at lower S/N are more compact than high-significance detections. On the other hand, González-López et al. (2018, in prep.) find that DSFGs at a few mJy (equivalent to ≥ 0.5 mJy at 1.1 mm) have compact sizes on average, with a median effective radius $\approx 0''.08$. For estimating the centroid coordinates of each source, we take the $S/N \geq 4.5$ pixel that established the detection, plus all surrounding pixels having $S/N \geq 4$. We collect the coordinates of these pixels, obtain the median right ascension and declination among all of them and set these median values as estimates of the source centroid coordinates.

Including these detections, our final catalog is comprised by 19 sources. We highlight that none of the $4.5 \leq S/N < 5$ sources are part of the lists of lensed galaxies used by the lens modeling teams, therefore they do not influence to the lens models.

2.2. Source redshifts

In a galaxy cluster field, the observed magnification by gravitational lensing of a background source varies with both its relative position and redshift. Since we have accurate positions and deep HST imaging, we thus consider available spectroscopic and photometric redshift information.

Laporte et al. (2017, hereafter Paper II) determine photometric redshifts for all our $S/N > 5$ detections via SED fitting, finding a mean redshift of $z = 1.99 \pm 0.27$. Five of these high-significance sources (A2744-ID01, A2744-ID02, MACSJ0416-ID01, MACSJ0416-ID02 and MACSJ1149-ID03) have spectroscopic redshifts from the GLASS survey (Treu et al. 2015), which are consistent with the photometric redshifts found. We

refer the reader to Paper II for more details regarding the multi-wavelength data used, photometry estimates and SED-fitting procedure.

We search for counterparts to our $4.5 \leq S/N < 5$ sources in several public catalogs reporting photometric and/or spectroscopic redshift estimates, including: photometric redshifts estimated by the CLASH team (Postman et al. 2012; Molino et al. 2017) and the ASTRODEEP survey (Castellano et al. 2016; Di Criscienzo et al. 2017); catalogs of spectroscopic redshifts by Owers et al. (2011), Ebeling et al. (2014), Jauzac et al. (2016), Kawamata et al. (2016), Treu et al. (2016), Mahler et al. (2018), the GLASS survey (Hoag et al. 2016), and the CLASH survey using VLT/VIMOS (Balestra et al. 2016) and VLT/MUSE (Grillo et al. 2016; Caminha et al. 2017); and redshift estimates for Herschel detections (Rawle et al. 2016). We find that only MACSJ0416-ID05 has a counterpart within $\approx 0''.3$ with a secure spectroscopic redshift $z = 1.849$. This was measured from NIR spectra as part of the GLASS survey, confirmed by fitting the continuum grism spectra to SED templates. This galaxy also has extensive multi-wavelength broadband data from ASTRODEEP and CLASH.

For the remaining $4.5 \leq S/N < 5$ sources, all galaxies in the aforementioned catalogs having reliable redshift estimates are beyond $\approx 1''$ from ALMA peak positions. In a few cases, these are contaminated by foreground sources. This makes identification of likely faint NIR emission particularly challenging, thus it is hard to gauge the veracity of these sources. For instance, MACSJ1149-ID03 has a counterpart within $\approx 0''.8$ with a very imprecise photometric redshift $z = 2.914 \pm 2.816$, obtained by the ASTRODEEP team via SED fitting to three NIR broadband filters (Keck-MOSFIRE Ks and Spitzer-IRAC 3.6 and 4.5). However, both MACSJ1149-ID03 and this ASTRODEEP source are close (within $\approx 1''.6$ and $\approx 0''.8$, respectively) to a star, securely identified by the GLASS survey using VLT/MUSE.

The choice of source redshifts is as follows. When available, we use spectroscopic redshifts. This includes five $S/N > 5$ and one $4.5 \leq S/N < 5$ detections respectively. These are presented in Table 1. For the remaining $S/N > 5$ sources, we use the photometric redshift probability distributions obtained in Paper II. In the aforementioned table, best fit values and 1σ errors from these distributions are presented for reference.

For sources lacking any redshift information (i.e. all but one $4.5 \leq S/N < 5$ sources), we assume a Gaussian redshift distribution centred at $z = 2$ with standard deviation 0.5. This assumption is supported by the mean photometric redshift found in Paper II for the $S/N > 5$ sources and by results from the literature found in blind mm detections reaching the sub-mJy level (e.g. Aravena et al. 2016; Dunlop et al. 2017). It is also consistent within $\approx 1\sigma$ with the median redshift of dusty galaxies at 1.1 mm predicted by Béthermin et al. (2015) using an empirical model, both including and not including strongly-lensed sources, for our chosen S/N threshold (assuming point sources).

2.3. Lensing models

A massive object (e.g. a galaxy cluster) deforms the space-time in its vicinity, acting as a gravitational lens (see Kneib & Natarajan 2011 for a review). In cluster fields, the light from background sources is deflected and magnified. Magnification estimates at each source position are essential for obtaining lensing-corrected flux densities and thus, the number counts. For this, we make use of gravitational lensing models produced by independent teams. Detailed explanations for the models (and their several versions) provided by each team can be found in the readme

Table 1. Continuum detections at $S/N \geq 4.5$.

ID	RA _{J2000} [hh:mm:ss.ss]	Dec _{J2000} [±dd:mm:ss.ss]	S/N	$S_{1.1\text{ mm, peak}}$ [mJy beam ⁻¹]	$S_{1.1\text{ mm, uv-fit}}$ [mJy]	z
A2744-ID01 ^a	00:14:19.80	-30:23:07.66	25.9	1.433 ± 0.056	1.570 ± 0.073	2.9 ^c
A2744-ID02 ^a	00:14:18.25	-30:24:47.47	14.4	1.292 ± 0.091	2.816 ± 0.229	2.482 ^c
A2744-ID03 ^a	00:14:20.40	-30:22:54.42	13.9	0.798 ± 0.058	1.589 ± 0.125	2.52 ^{+0.23d} _{-0.45}
A2744-ID04 ^a	00:14:17.58	-30:23:00.56	13.8	0.932 ± 0.068	1.009 ± 0.074	1.02 ^{+0.32d} _{-0.09}
A2744-ID05 ^a	00:14:19.12	-30:22:42.20	7.7	0.655 ± 0.086	1.113 ± 0.135	2.01 ^{+0.69d} _{-0.16}
A2744-ID06 ^a	00:14:17.28	-30:22:58.60	6.5	0.574 ± 0.089	1.283 ± 0.241	2.08 ^{+0.13d} _{-0.08}
A2744-ID07 ^a	00:14:22.10	-30:22:49.67	6.2	0.455 ± 0.074	0.539 ± 0.082	1.85 ^{+0.16d} _{-0.14}
A2744-ID08 ^b	00:14:24.73	-30:24:34.20	4.8	0.270 ± 0.056
A2744-ID09 ^b	00:14:21.23	-30:23:28.70	4.7	0.256 ± 0.055
A2744-ID10 ^b	00:14:17.72	-30:23:02.25	4.5	0.286 ± 0.063
A2744-ID11 ^b	00:14:22.63	-30:23:30.45	4.5	0.253 ± 0.056
MACSJ0416-ID01 ^a	04:16:10.79	-24:04:47.53	15.4	1.010 ± 0.066	1.319 ± 0.103	2.086 ^c
MACSJ0416-ID02 ^a	04:16:06.96	-24:03:59.96	6.8	0.406 ± 0.062	0.574 ± 0.132	1.953 ^c
MACSJ0416-ID03 ^a	04:16:08.81	-24:05:22.58	5.8	0.389 ± 0.067	0.411 ± 0.072	1.29 ^{+0.11d} _{-0.39}
MACSJ0416-ID04 ^a	04:16:11.67	-24:04:19.44	5.1	0.333 ± 0.066	0.478 ± 0.166	2.27 ^{+0.17d} _{-0.61}
MACSJ0416-ID05 ^b	04:16:10.52	-24:05:04.77	4.6	0.302 ± 0.066	...	1.849 ^e
MACSJ1149-ID01 ^a	11:49:36.09	+22:24:24.60	5.9	0.442 ± 0.074	0.579 ± 0.134	1.46 ^c
MACSJ1149-ID02 ^b	11:49:40.32	+22:24:42.00	4.6	0.524 ± 0.113
MACSJ1149-ID03 ^b	11:49:35.41	+22:23:38.60	4.5	0.326 ± 0.072

Notes. Column 1: Source ID. Columns 2, 3: Centroid J2000 position of ID. Column 4: Signal-to-noise of the detection. Column 5: PB-corrected peak intensity and 1σ error. Column 6: PB-corrected integrated flux density and 1σ error from uv fitting. Column 7: Source redshift. ^(a) High-significance ($S/N \geq 5$) detections. Already reported in Paper I. ^(b) Low-significance ($4.5 \leq S/N < 5$) detections. Instead of performing a uv fitting, we adopt the peak intensity as the best estimate of the integrated flux density for these sources. Since all but one of them lack clear counterparts (partly due to contamination) and spectroscopic redshifts, nor were they included in Paper II study, we assume a Gaussian redshift distribution with mean $z = 2$ and $\sigma = 0.5$ for these sources. ^(c) Spectroscopic redshift from GLASS, already noted in Paper II. ^(d) Photometric redshift found in Paper II. Best fit value and 1σ error from SED fitting are presented here only for reference, as we use the full probability distribution found for each photometric redshift. ^(e) Spectroscopic redshift from GLASS.

Table 2. Lensing models considered in this work.

Model	References
Caminha v4 ^a	Caminha et al. (2017)
CATS v4, v4.1	Jullo & Kneib (2009); Richard et al. (2014); Jauzac et al. (2014, 2015, 2016)
Diego v4, v4.1	Diego et al. (2005, 2007, 2015)
Keeton v4	Keeton (2010); Ammons et al. (2014); McCully et al. (2014)
Sharon v4	Jullo et al. (2007); Johnson et al. (2014)
Williams v4	Liesenborgs et al. (2006, 2007); Sebesta et al. (2016)

Notes. All these models cover the region where our ALMA sources lie. ^(a) Only available for MACSJ0416.

files publicly available in the FF website¹. In the following, different model versions from a given team are treated as separated models.

Each modeling team uses their own choice of assumptions and methods. Lensing mass inversion techniques include parametric, free-form (or “non-parametric”) and hybrid (i.e. a mixture of both) models. Parametric models, as the name suggests, assume that the mass distribution can be represented by a superposition of analytical functions that depend on a limited number of free parameters. In most cases, these models are guided by the distribution of cluster members and their luminosities. Free-form models do not use this assumption, but find the solution directly from the multiple-image constraints (as a result, their resolution is often lower). Parametric models include Caminha (Caminha

et al. 2017), CATS (Jullo & Kneib 2009; Richard et al. 2014; Jauzac et al. 2014, 2015, 2016), Keeton (Keeton 2010; Ammons et al. 2014; McCully et al. 2014) and Sharon (Jullo et al. 2007; Johnson et al. 2014). Williams (Liesenborgs et al. 2006, 2007; Sebesta et al. 2016) is a free-form model, while Diego (Diego et al. 2005, 2007, 2015) is hybrid. Brief descriptions of these and more models can be found in Coe et al. (2015) and Priewe et al. (2017).

Table 2 lists the models considered in this work. These models are constrained by input archival observations (both from HST and ground based), redshifts and multiple image identifications. The reliability of these constraints has been collectively assigned by all teams, ranking each constraint as Gold, Silver or Bronze (see Priewe et al. 2017). Model versions v3 and newer are based on FF observations, with v4 and newer models using a

¹ <http://archive.stsci.edu/prepds/frontier/lensmodels/>

considerably larger set of arcs and spectroscopic redshifts compared to previous versions. Model versions v4 and v4.1 vary in the set of constraints chosen by each team, with v4 models using only the most reliable constraints (i.e. images from the Gold sample²). For details regarding the selection of constraints and their reliability, we refer to the readme files publicly available for each lens model. We attempt to use the best data to date, so for all cluster fields we consider only v4 or newer models.

Lens models are comprised of maps of the normalized mass surface density κ and shear γ of the galaxy cluster, assuming a redshift $z = \infty$ background. The deflection field $\vec{\alpha}$ around the lensing object can be estimated from κ as

$$\nabla \cdot \vec{\alpha} = 2\kappa \quad (1)$$

(Coe et al. 2008). These maps are scaled to the source-plane z of interest as

$$\kappa(z) = \kappa \frac{D_{LS}}{D_S}, \quad \gamma(z) = \gamma \frac{D_{LS}}{D_S}, \quad \vec{\alpha}(z) = \vec{\alpha} \frac{D_{LS}}{D_S}, \quad (2)$$

where the angular diameter distances D_S and D_{LS} are computed from source to observer and source to lens respectively. The magnification map at a given source-plane z is obtained as (see Coe et al. 2015)

$$\mu(z) = \frac{1}{|(1 - \kappa(z))^2 - \gamma(z)^2|}. \quad (3)$$

For each release, teams provide a lens model coined as “best”, plus a range of individual reconstructions (hereafter the “range” maps) that sample the range of uncertainties, i.e. there is one κ and γ map for each realization. The field of view and angular resolution adopted for presenting the maps, as well as the number of realizations provided, may vary across teams and model versions.

We use the full set of mass reconstructions for estimating uncertainties in both source magnifications and effective source-plane areas in a given lens model. These in turn are propagated to the number counts as explained in §3. In order to use the models, “range” maps for κ and γ are reprojected to the size and resolution of the ALMA maps using a first order interpolation. Based on these, we can obtain magnification maps for a given source redshift using Eq. 3. However, we adopt redshift probability distributions for most of the detections (see §2.2), and therefore need to make these calculations for several redshift values. In order to make our Monte Carlo simulations faster, we precompute magnification maps for a fixed grid in redshift, using steps of $\Delta z = 0.2$ in the range $z_{\min} = 0.4$ to $z_{\max} = 4$ for A2744 and MACSJ0416 ($z_{\min} = 0.6$ for MACSJ1149, given the higher cluster redshift). It is safe to consider only this redshift range since it contains all the adopted spectroscopic redshifts; also, all our photometric redshift distributions have zero values at $z \geq 4$, and this limit is at 4σ from the mean redshift assumed for sources lacking redshift information.

² Note, however, that the choice of constraints for v4 models is not completely homogeneous across teams. For instance, Sharon included also few Silver and Bronze images in regions where the number of Gold images is small. Similarly, teams that released v4.1 versions added particular lower-ranked constraints: CATS added Silver images plus some very (photometrically) convincing candidates, while Diego added the full Silver and Bronze sets.

Across the Monte Carlo simulations, we approximate sample redshifts to their closest redshift bins, and use the corresponding sets of precomputed magnification maps. It is safe to use this approximation even for sources having spectroscopic redshifts, as we check that the predictions using their two closest redshift bins have no significant variation for most detections. In some lens models, however, the variation of source magnification with redshift is not smooth for A2744-ID09 and A2744-ID11, as for certain redshifts they lie close to cluster critical lines (i.e. where magnification formally diverges). These sources lack redshift information, making it difficult to constrain the source magnification. Nevertheless, the predictive power of lens models is lower close to critical lines (see §3.3), and thus these sources have little accuracy in their magnifications anyway.

All v4 and v4.1 lens models cover the region where our detections lie. However, a fraction of the region where the ALMA maps have $PB > 0.5$ is not fully covered by the Williams v4 model: $\sim 2\%$, 13% and 5% for A2744, MACSJ0416 and MACSJ1149, respectively. In these cases, we impose $\mu = 1$ for the missing pixels in magnification maps. In total, we adopt for use seven, eight and seven lens models for A2744, MACSJ0416 and MACSJ1149, respectively (see Table 2). Deflection field maps are needed to “delens” the magnification maps and in turn compute effective source-plane areas for each detection. Not all modelers provide these maps for all realizations, so we use Eq. 1 to compute the deflection field maps from the κ maps provided for the “range” models.

3. Methodology

We compute demagnified number counts at 1.1 mm. This requires recovering the demagnified (i.e. source-plane) integrated flux density S_{demag} for each source, which is obtained as

$$S_{\text{demag}} = \frac{S_{\text{obs}}}{\mu}. \quad (4)$$

Here, S_{obs} corresponds to the measured (i.e. image-plane) integrated flux density and μ the source magnification (see §3.3). We obtain the differential number counts at the j -th flux density bin as

$$\frac{dN}{d \log(S)} = \frac{1}{\Delta \log(S)} \sum_i^n X_i, \quad (5)$$

where we sum the individual contribution X_i to these counts by the sources that have flux densities $S_{j-(\Delta \log(S))/2} \leq S_{\text{demag},i} < S_{j+(\Delta \log(S))/2}$. Similarly, we compute the cumulative number counts for the k -th flux limit as

$$N(> S_k) = \sum_i^m X_i, \quad (6)$$

where we sum over the sources having $S_{\text{demag},i} \geq S_k$. In these two expressions, we estimate the contribution by the i -th source as

$$X_i = \frac{1 - p_{\text{false},i}}{C_i A_{\text{eff},i}}. \quad (7)$$

Here, C_i is a completeness correction (see §3.1) and $p_{\text{false},i}$ the probability of a spurious detection (see §3.2). $A_{\text{eff},i}$ corresponds

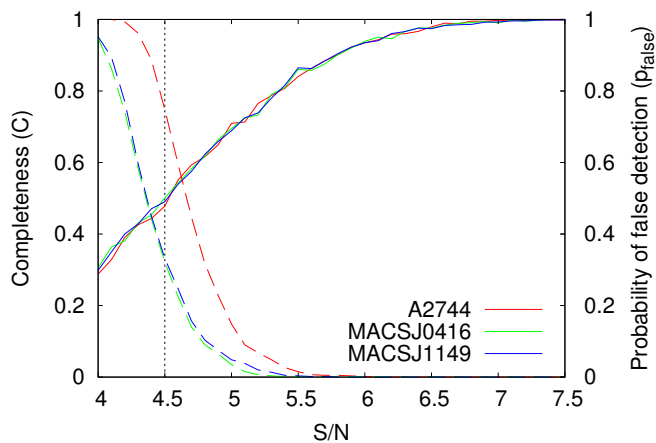


Fig. 1. Completeness correction C (solid lines) and probability of false detection p_{false} (dashed lines) as a function of S/N . We display curves for A2744, MACSJ0416 and MACSJ1149 in red, green and blue respectively. A vertical dotted black line indicates our S/N threshold of 4.5.

to the effective area where that source can be detected (see §3.5), depending on the source redshift and lens model that is adopted.

A detailed treatment for all these quantities is described in this section. Throughout our number count analysis, we consider ALMA detections down to $S/N = 4.5$. This S/N threshold is chosen as an appropriate balance between the correction factors that are related to the source detection, even when the level of false detection probability is not homogeneous among cluster fields (see §3.2).

For the sake of simplicity, we assume that none of the ALMA continuum detections are multiply imaged over the S/N threshold. We verified this for all lens models using their “best” maps (see §2.3). For each ALMA detection, we create a set of image-plane mosaic pixels, comprised by its peak plus all the $S/N \geq 4$ pixels surrounding it (hereafter Set 1). For a given lens model and redshift, we use the deflection fields for finding the spatial coordinates of Set 1 pixels in the source plane. We later search for all the image-plane pixels that are deflected from these source-plane coordinates. This new set includes Set 1 pixels (by construction) but may include new mosaic positions if the source-plane pixels are multiply imaged. If any of these new pixels belongs to any of the remaining ALMA detections, i.e. matches another peak pixel or a $S/N \geq 4$ pixel surrounding it, a detection is said to be multiply imaged (above the S/N threshold) in our mosaics.

Adopting the same redshift bins as when precomputing magnification maps, we find that none of our $S/N \geq 4.5$ detections are a multiple image of another one in the catalog. Moreover, we check that none of the newly found image-plane positions have $S/N \geq 4$. Therefore, if any of our detections both lies at one of the redshifts considered and is multiply imaged, then the predicted images could not be detected, unless a $S/N < 4$ criterion is used. We further assume that we have recovered the total 1.1 mm flux densities, within their respective errors.

3.1. Completeness

In presence of noisy data, number counts need to be corrected by the proportion of sources that were not detected, because their noise level shifted their peak S/N below our chosen threshold.

We compute the completeness as a function of S/N as follows. We draw 3×10^5 artificial image-plane point sources from a flat peak intensity distribution in the range $0.05 - 3 \text{ mJy beam}^{-1}$. This interval is chosen based on the peak intensities and their 1σ errors in our source catalog. One at a time, we inject these sources randomly in a PB-corrected, simulated noise map (see §3.2). We later obtain their extracted peak S/N from the non-PB-corrected peak intensities at the source positions, and check if these meet our S/N criterion. We restrict this source injection only to the $PB > 0.5$ region. We obtain the completeness C for each (injected) S/N bin as the fraction of sources that have an (extracted) $S/N \geq 4.5$ and are thus detected. We adopt this procedure using both positive (i.e. true) and negative (i.e. inverted) noise maps in each cluster field, and average the corresponding C values per S/N bin. This average is taken for reducing the scatter in the completeness curve (results for positive and negative maps at a given S/N vary by up to $\sim 5\%$). The completeness corrections for all cluster fields are shown in Fig. 1. At $S/N = 4.5$, the completeness is around 0.5 for all cluster fields. At $S/N = 6.7$, the sample is 99% complete in S/N .

Since our source catalog is S/N limited, we note that measured source intensities may be systematically enhanced by noise fluctuations, such that they are boosted over the S/N threshold and thus bias the number counts. Correcting by this effect is known as flux deboosting (e.g. Hogg & Turner 1998; Weiß et al. 2009). We choose to make no assumptions regarding the true underlying distribution of flux densities, and therefore do not apply any deboosting correction. This is supported by the low number density of ALMA sources in the FFs.

We choose to make no assumptions regarding the intrinsic size distribution at low flux densities, so our methodology may be biased against detecting extended sources. For high magnifications and/or large intrinsic source sizes, this may lead to magnified images being larger than the synthesized beam (thus missed in the observation) and/or peak intensities below our chosen S/N threshold (thus missed in the detection criterion). Accounting for these effects could elevate the derived number counts at low flux densities, and so we expect to include them in future work. However, recent observational results suggest on average relatively small sizes for the dust emission in ALMA detections at low flux densities (e.g. Fujimoto et al. 2017 and González-López et al. 2018 in prep., see §2.1.2).

3.2. Probability of false detection

We compute the probability that a detection is spurious (i.e. generated by noise) as a function of S/N as follows. For each galaxy cluster field, we generate 300 simulated non-PB-corrected maps, having the same size and resolution as the true ALMA mosaics. Each fake map is comprised by pure Gaussian noise with mean 0 and variance 1 (in S/N units), convolved with the ALMA synthesized beam. We extract sources from each simulated map just as done with the true maps (see Paper I). We compute the probability of a false detection, p_{false} , as the fraction of simulated maps where at least one source is detected over that peak S/N . As for C , we obtain these curves using positive and negative mosaics separately. We adopt the average p_{false} value per S/N limit.

Fig. 1 shows the probability of a false detection at a given S/N for the three clusters. The S/N values at which a detected source has 50% chance of being false are ≈ 4.7 for A2744 and ≈ 4.4 for MACSJ0416 and MACSJ1149. Below $S/N \approx 4.3$, eventually all sources detected in the A2744 mosaic are expected to be spurious, while at the same S/N the probability is about 60% for the remaining cluster fields. At $S/N = 4.5$, the chance

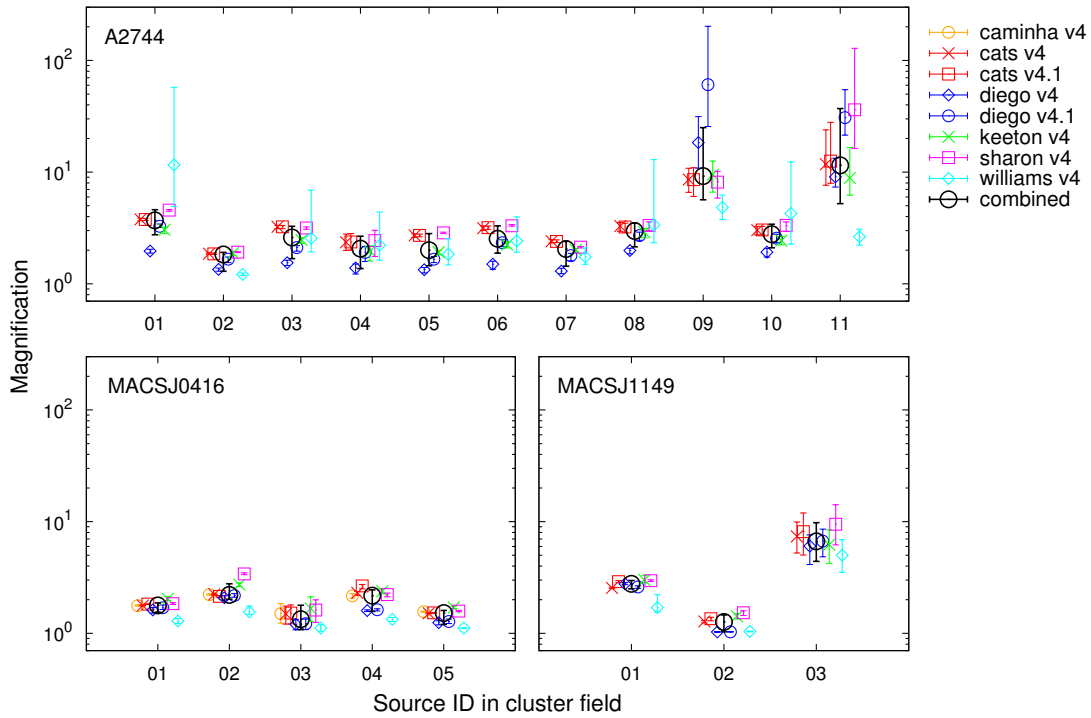


Fig. 2. Median magnification per source for the lens models listed in Table 2 (colored symbols), and also combining all models for each cluster field (large black circles). Error bars indicate the 16th and 84th percentiles (see §3.3). Values for each model have been offset around the source ID for clarity.

is about 70% for A2744 and 30% for both MACSJ0416 and MACSJ1149. We note that above $S/N \approx 4.8$, the completeness correction plays a greater role over the contamination by spurious sources in A2744 (see Eq. 7). For the remaining cluster fields, this happens at $S/N \approx 4.4$.

The clear difference of the A2744 curve from the other cluster fields comes from the smaller synthesized beam in the A2744 map ($0''.63 \times 0''.49$) compared to the MACSJ0416 and MACSJ1149 mosaics ($1''.52 \times 0''.85$ and $1''.22 \times 1''.08$ respectively). From Gaussian statistics, having more independent beams contained in a map enhances the probability of finding larger noise values across the mosaic. Therefore, noise values are mistaken for true extragalactic signal more often in A2744 than in the remaining galaxy clusters.

3.3. Source magnifications

Predicting how much is the source brightness amplified by the gravitational lensing effect is necessary for estimating the intrinsic emission from background sources. Lens models applying different techniques predict different values for that magnification.

The centroid pixel of each ALMA detection (see §2.1), together with the “range” maps (see §2.3), are used to calculate the magnification for each source. Indeed, we obtain the magnification distribution for a given source and lens model using the μ values found for the source centroid pixel in all the “range” maps. This choice implies neglecting the effects of differential magnification, and is done in order to simplify the calculations. This is safe as most detections lie far from critical lines, thus magnifications do not have a strong variation across the image-plane extension of these sources. Moreover, the few detections that are found closer to critical lines have very few pixels with

$S/N \geq 4$ (up to seven pixels in A2744 and 15 in MACSJ1149), over which the magnification does not vary strongly either (for a given “range” map).

Since we are adopting a non-unique redshift, we use a Monte Carlo approach with 1000 realizations. Each time, we draw a random z value from the source redshift probability distribution (see §2.2), and resample the source magnification distribution corresponding to that redshift to obtain a μ value. In order to speed up these calculations, we approximate the random z to the closest value used in our set of precomputed magnification maps (see §2.3). If a sample z is lower than the cluster redshift (e.g. the photometric redshift distribution has a non-zero probability which extends below the cluster redshift), we assume $\mu = 1$ for the source, use its observed flux density and compute the corresponding effective area in the image plane (i.e. assuming all map pixels have $\mu = 1$). This happens only to sources A2744-ID03 and A2744-ID04 and at a very low rate ($\sim 3\%$ and $< 1\%$ of the realizations, respectively), thus the inclusion of photometric redshift tails below the cluster redshift has a negligible impact in our results.

The magnification distribution sampled for each source is then a combination of distributions obtained at the source position for several redshifts. From this sampling, we can compute a median magnification for each source and estimate uncertainties using the 16th and 84th percentiles (following Coe et al. 2015). This is shown in Fig. 2 for the models listed in Table 2, and also combining all models for each cluster field. Median (combined) magnification values for our sample range from 1.3 to 11.5.

In a given lens model, we find that sources having higher median magnifications have also larger dispersions. Some sources having median $\mu \gtrsim 10$ reach dispersions $\gtrsim 0.5$ dex, e.g. sources A2744-ID09 in the Diego v4.1 model and A2744-ID11 in the Sharon v4 model. Magnification distributions are broad and

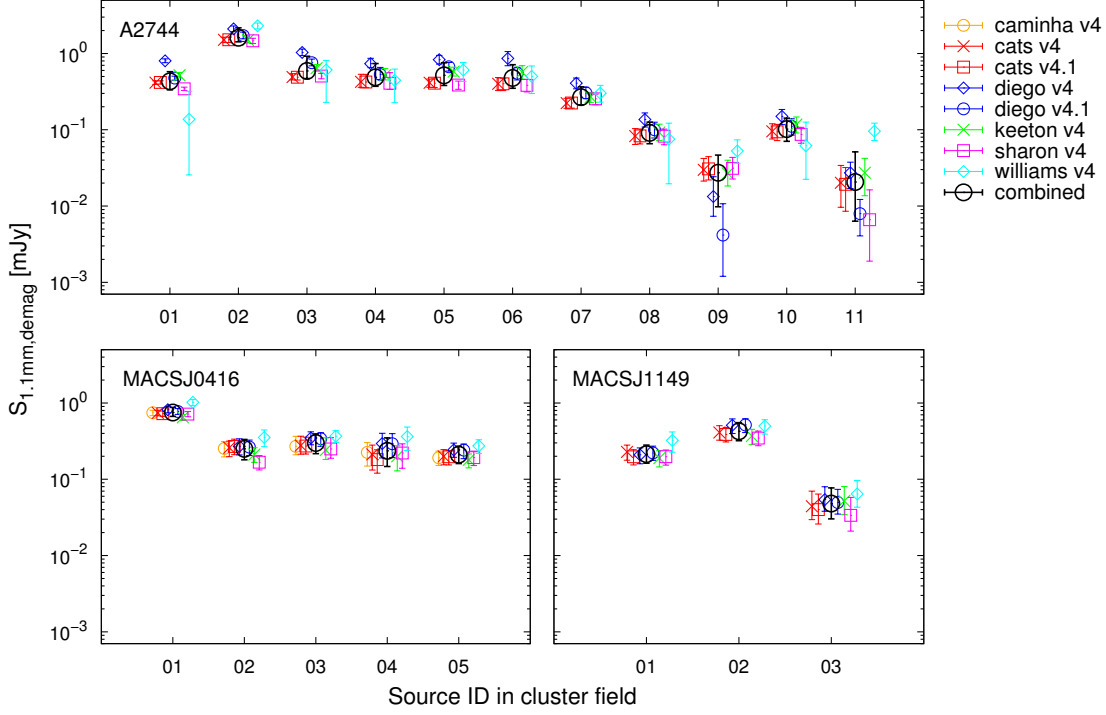


Fig. 3. Median demagnified integrated flux density per source for the lens models listed in Table 2 (colored symbols), and also combining all models for each cluster field (large black circles). Error bars indicate the 16th and 84th percentiles. Values for each model have been offset around the source ID for clarity.

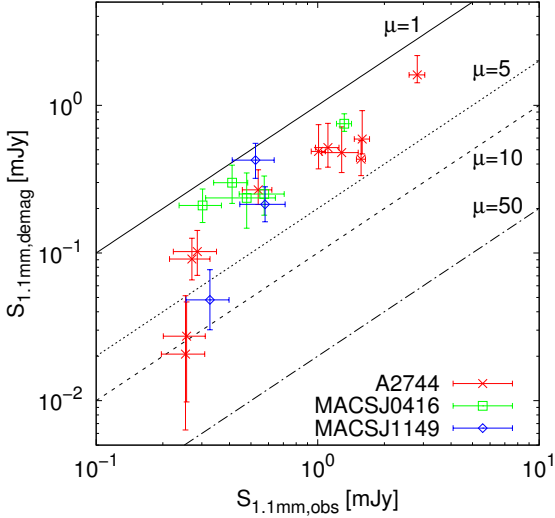


Fig. 4. Median demagnified integrated flux density as a function of observed integrated flux density for A2744 (red crosses), MACSJ0416 (green squares) and MACSJ1149 (blue diamonds). Median values are obtained combining all models for each cluster field. Error bars in demagnified fluxes correspond to the 16th and 84th percentiles while for observed fluxes are 1σ statistical uncertainties. As a reference, black lines indicate magnification values of 1 (solid), 5 (dotted), 10 (dashed) and 50 (dot-dashed).

asymmetrical for sources A2744-ID01, A2744-ID03, A2744-ID04, A2744-ID08 and A2744-ID10 in the Williams v4 model, although most of them have median $\mu < 10$. Sources in

MACSJ0416 have very similar magnifications in all models, showing small individual dispersions.

Previous works have used the lens models publicly available in the FFs for quantifying systematic uncertainties in predicted magnifications, applying the lens models both to observations (e.g. Bouwens et al. 2017, Lotz et al. 2017, Priewe et al. 2017) and simulations (e.g. Johnson & Sharon 2016, Acebron et al. 2017, Meneghetti et al. 2017). Our trend of increasing dispersion with source magnification (see Fig. 2) is in line with results by Zitrin et al. (2015), Meneghetti et al. (2017) and Bouwens et al. (2017). Zitrin et al. (2015) presented a comprehensive lensing analysis of the complete CLASH cluster sample, examining several lens models produced by their team. They found that the systematic differences (relative to one of the models) increase rapidly with the magnification value. Meneghetti et al. (2017) made a detailed comparison of the mass reconstruction techniques applied by different teams using two simulated galaxy clusters, which resemble the depth and resolution of the FFs. They found that the largest uncertainties in lens models are close to cluster critical lines, with the predictive power of the lens models worsening at $\mu > 10$. For instance, they estimated that the accuracy in the magnifications predicted by some models degrades from $\sim 10\%$ at $\mu = 3$ to $\sim 30\%$ at $\mu = 10$. Bouwens et al. (2017) found similar results using a sample of 160 lensed, NIR-detected sources at $z \sim 6$ in the first four FFs. They constrained the faint end of the $z \sim 6$ ultraviolet luminosity function (UV LF), finding systematic variations in the LF of several orders of magnitude at $M_{UV,AB} = -12$ mag and fainter. They attributed this to the large systematic uncertainties inherent at high magnifications, with models having a poor predictive power specially at $\mu > 30$.

Furthermore, Lotz et al. (2017) computed method-to-method standard deviations for the subset of models in A2744 and

MACSJ0416 that kept using the same methodology across versions (i.e. for both pre- and post-FF data). They found no significant reduction in the magnification variations across methodologies, reporting median systematic uncertainties in magnification of $< 26\%$ and 15% , for v3 models in A2744 and MACSJ0416, respectively. However, Priewe et al. (2017) found a systematic uncertainty of 70% at $\mu \sim 40$, using the dispersion between v3 or newer lens models in those cluster fields for a $z = 9$ source plane. They argued that the discrepancies in the magnification predictions among models, which often exceed the statistical uncertainties reported by individual reconstructions, were driven by lensing degeneracies, i.e. different mass distributions may reproduce the same observational constraints. Moreover, they found the Williams v3 model gives the largest magnification uncertainties at most sky locations in A2744. The broad magnification distributions that we find for some sources in A2744 in the Williams v4 model (see Fig. 2) are in line with these findings.

3.4. Lensing-corrected source flux densities

Once the magnification distribution for each source is obtained, the demagnified integrated flux density is recovered using Eq. 4 for the different lens models. We do this by adopting a Gaussian distribution for S_{obs} with standard deviation given by its reported statistical error, and the distribution described in §3.3 for the magnification. Using both, we resample 1000 times the ratio given in Eq. 4 to obtain a distribution for S_{demag} .

Fig. 3 shows the median demagnified integrated flux density for each source, computed from both the distributions obtained for each model and joining all of them for each cluster field. Median (combined) lensing-corrected flux densities range from ~ 0.02 to 1.61 mJy, with both the faintest and brightest sources in the sample being found around A2744. Naturally, sources having broad magnification distributions have also large uncertainties in their median S_{demag} values. Within the uncertainties, combined demagnified flux densities cover around 2.5 orders of magnitude.

At $S_{\text{obs}} \gtrsim 0.4$ mJy, we find a trend of brighter observed sources being also brighter intrinsically, while sources having lower observed flux densities tend to span ≈ 1.5 dex in demagnified flux. This is shown in Fig. 4. We also find that sources with the highest magnifications ($\mu \gtrsim 5$) are among the faintest ones both in observed and lensing-corrected flux ($S_{\text{obs}} \lesssim 0.4$ mJy and $S_{\text{demag}} \lesssim 0.06$ mJy, respectively).

3.5. Source effective areas

For computing counts, a key step is to estimate the effective area, A_{eff} , over which the source can be detected. That is, the angular area in the source plane where a map pixel having a given peak intensity can be detected over a given S/N threshold. The effective area at a given demagnified peak intensity depends not only on the PB response, but also on the source redshift assumed and the lens model adopted.

At a given redshift, we estimate the effective area as a function of demagnified peak intensity $S_{\text{demag,peak}}$ (corrected for PB attenuation) as follows. We consider a PB-corrected rms map for each cluster. For each “range” map in a given lens model, we deflect both the PB-corrected rms and magnification maps to the source plane using the deflection fields (see §2.3). If several pixels in the image plane are deflected to only one in the source plane, only the image-plane pixel with the highest magnification is kept and assigned to the source-plane pixel (following Coe

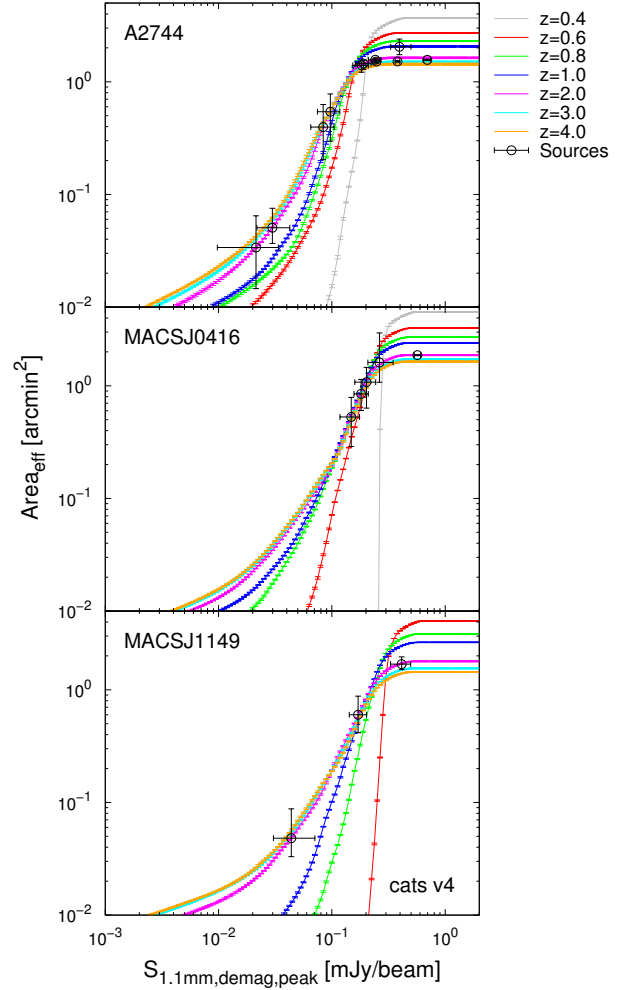


Fig. 5. Median effective area as a function of demagnified peak intensity at several redshifts as indicated in the key (colored lines) for the CATS v4 lens model. Values for our $S/N \geq 4.5$ sources (black symbols) are shown for this model (corresponding to the red crosses in Fig. 6). Error bars indicate the 16th and 84th percentiles. For each curve, these are obtained using the “range” maps at the corresponding redshift, while for symbols they are computed as described in §3.5. At $z \geq 2$, areas do not differ significantly with redshift for this lens model.

et al. 2015). The lensing-corrected rms level for each source-plane pixel, σ_{demag} , is then given by the ratio between its PB-corrected rms and magnification. At a given $S_{\text{demag,peak}}$, we collect all the source-plane pixels where $S_{\text{demag,peak}}/\sigma_{\text{demag}} \geq 4.5$. The effective area corresponds to the sum of source-plane pixels meeting this criterion, each of them given by the ALMA mosaic resolution. We precompute A_{eff} vs $S_{\text{demag,peak}}$ curves for each of the redshifts used in our set of precomputed “range” magnification maps (see §2.3).

For each source, we use its full distribution of demagnified peak intensities to compute its effective area. We obtain the $S_{\text{demag,peak}}$ distribution as in §3.4, but using a Gaussian distribution for the image-plane peak intensity $S_{\text{obs,peak}}$ instead of S_{obs} . We perform a Monte Carlo simulation where we use the same number of realizations and follow the same approach for obtaining both random $S_{\text{obs,peak}}$ and z values as in §3.3. This time, however, we need to resample directly the set of “range” magnification maps, in such a way that the same magnification map is used for obtaining both $S_{\text{demag,peak}}$ and A_{eff} . This is required in order

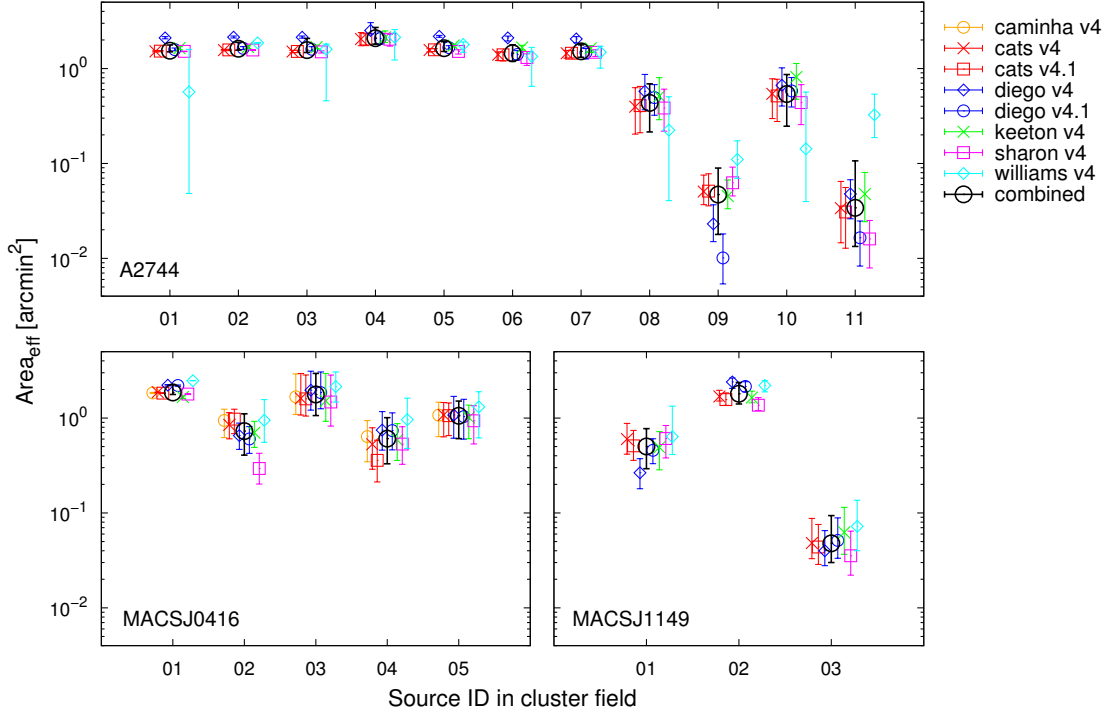


Fig. 6. Median effective area per source for the lens models listed in Table 2 (colored symbols), and also combining all models for each cluster field (large black circles). Error bars indicate the 16th and 84th percentiles. Values for each model have been offset around the source ID for clarity.

to have consistency between their values, since both depend on μ values (of the source centroid pixel and all $PB > 0.5$ pixels, respectively) in an individual “range” map.

This resampling is done using the “range” map identifiers, which are numbered from 0 to $N_{\text{range}} - 1$ (with N_{range} the number of “range” maps provided for each model). We draw a random “range” map identifier using a uniform distribution bounded by 0 and $N_{\text{range}} - 1$. Using the “range” map corresponding to that identifier, we obtain the source magnification in the realization. We then use Eq. 4 for computing the source demagnified peak intensity, and then linearly interpolate the precomputed A_{eff} vs $S_{\text{demag,peak}}$ curve for that “range” map to estimate the source effective area.

The mass reconstruction for each cluster and lens model predicts a distinct proportion between high- μ and low- μ pixels at a given redshift. This is the main driver shaping the slope of the A_{eff} vs $S_{\text{demag,peak}}$ curve. Finding small effective areas at low demagnified peak intensities is a natural consequence of having few regions in the maps with very high magnification. In general, the effective area increases steeply with peak intensity until some point where it reaches a plateau. In a given model, both the slope at low peak intensities and plateau level at high peak intensity depend on the modelled cluster field and adopted source redshift.

We illustrate this in Fig. 5 for the CATS v4 model. At $z = 2$, for instance, the largest effective areas found are $1.63^{+0.02}_{-0.02}$, $1.87^{+0.01}_{-0.02}$ and $1.79^{+0.02}_{-0.01}$ arcmin² for A2744, MACSJ0416 and MACSJ1149, respectively. They sum to a total effective area of ≈ 5.3 arcmin². This source-plane area is around 2.6 times smaller than the total image-plane coverage (see §2.1.1). In the low peak intensity regime, lower source redshifts give smaller effective areas, while at $S_{\text{demag,peak}} \gtrsim 0.2$ mJy beam⁻¹ the opposite occurs. At $0.06 - 0.1$ mJy beam⁻¹, the steepness of the A_{eff} vs $S_{\text{demag,peak}}$ curves in a log-log scale are such that uncertain-

ties of e.g. 0.2 dex in source peak intensity lead to uncertainties around 0.5 dex in source effective area. However, the curves become shallower below 0.06 mJy beam⁻¹, giving a scatter in effective area of around the same order of magnitude (or below) than that in peak intensity. We find a similar qualitative behavior in the rest of the lens models used in this work, changing the numbers in the aforementioned effective areas and peak intensities.

Fig. 6 shows the median effective area for each source, computed from both the distributions obtained for each model and joining all of them for each cluster field. Median (combined) effective areas range from ~ 0.03 to 2.1 arcmin². Within the uncertainties, combined effective areas cover around 2.5 orders of magnitude. In Fig. 7, we compare the uncertainties in the (combined) median S_{demag} and A_{eff} values for our sources. In the bright end ($\gtrsim 0.3$ mJy) we find that sources lie at the A_{eff} plateau, thus uncertainties in effective areas are less affected by uncertainties in S_{demag} and more by the scatter across lens models. At $\approx 0.06 - 0.3$ mJy, sources with a S_{demag} error of e.g. 0.3 dex have an A_{eff} error close to 0.5 dex. Below 0.06 mJy, uncertainties in both of those quantities remain comparable in terms of order of magnitude, reaching even 1 dex.

3.6. Monte Carlo simulation for source counts

We combine the techniques explained in previous sections to estimate demagnified source counts that take into account the uncertainties in observed flux densities (see Table 1), adopted redshifts and modelled magnifications. We achieve this using a Monte Carlo approach. A diagram for the way in which this Monte Carlo simulation runs is shown in Fig. 8. For a given galaxy cluster field and lens model, we run a total of 1000 realizations. In each of them, we compute the number counts as follows.

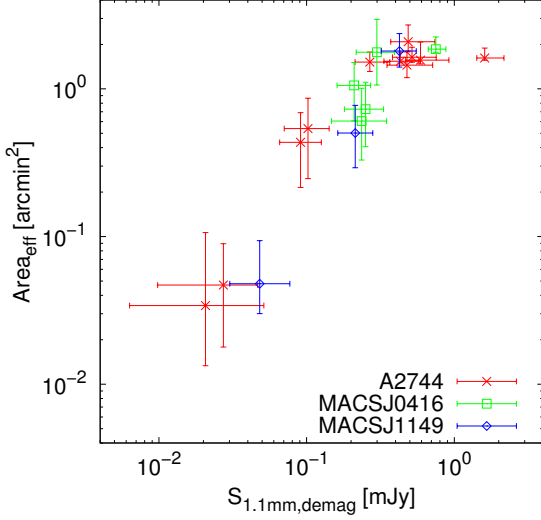


Fig. 7. Median effective area as a function of demagnified integrated flux density for A2744 (red crosses), MACSJ0416 (green squares) and MACSJ1149 (blue diamonds). Median values are obtained combining all models for each cluster field. Error bars correspond to the 16th and 84th percentiles. For comparing uncertainty values, both axes cover the same interval in order of magnitude. Within the errors, both demagnified flux densities and effective areas span around 2.5 orders of magnitude.

We generate a simulated source catalog comprised of 19 sources, keeping the same coordinates as the true detections. For each source i , we draw a random observed integrated flux density $S_{\text{obs},i}$ from a Gaussian distribution centred at S_{obs} with standard deviation δS_{obs} ; we proceed similarly for obtaining a random observed peak intensity $S_{\text{obs,peak},i}$. We also draw a random redshift from the source redshift probability distribution (see §2.2), and use its approximated value z_i as described in §3.3. We then draw a random magnification μ_i as in §3.5, i.e., using the identifiers of the “range” maps at the selected z_i (and keeping a record of the selected map identifier). We also obtain the source signal-to-noise ratio as $(S/N)_i = S_{\text{obs,peak},i} / \delta S_{\text{obs,peak}}$, and in the following consider only sources having $(S/N)_i \geq 4.5$. We then use Eq. 4 to obtain the demagnified integrated flux density and peak intensity ($S_{\text{demag},i}$ and $S_{\text{demag,peak},i}$) from S_{obs} , $S_{\text{obs,peak},i}$ and μ_i . We also obtain the completeness correction C_i and probability of a spurious detection $p_{\text{false},i}$ at the source $(S/N)_i$, interpolating the curves computed in §3.1 and §3.2 (see Fig. 1). Recalling the selected map identifier at z_i , we obtain the effective area $A_{\text{eff},i}$ at the source $S_{\text{demag,peak},i}$ interpolating the curves precomputed in §3.5.

Having all the needed properties, we compute the differential and cumulative number counts using Eqs. 5 to 7. We adopt $\Delta \log(S) = 0.5$ and use the same flux limits for all realizations, in order to combine them later. We follow this procedure for all lens models and cluster fields. Using a given lens model, the set of realizations samples the probability distribution for the number counts in each flux bin, such that we can compute median number counts per flux bin. However, for estimating the associated uncertainties, in this case, we need to take into account low number statistics. We achieve this by computing, besides the 16th and 84th percentiles in the counts per flux bin, the Poisson confidence levels for 1σ lower and upper limits. These levels are provided by Gehrels (1986) as a function of the number of

events, which in our case is the median number of sources per flux bin.

We compute combined differential counts taking the median value per flux bin over a subset of lens models. For each flux bin, the chosen subset includes the models where at least one realization has non-zero differential counts, so we avoid models that give zero probability of counts per flux bin. We use this to combine the counts in each cluster field separately, where the subset considers only models available for that particular field (see Table 2), as well as to combine the counts across all cluster fields, where the subset covers models in all fields. For computing combined cumulative counts, we take the median value per flux density limit. In this case, the subset of models includes those where at least one realization has non-zero cumulative counts.

4. Results and Discussion

4.1. Number counts

Table 3 lists the median differential and cumulative counts, combining models for each cluster field both separately and altogether. Uncertainties in the counts are obtained from the 16th and 84th percentiles, listed together with the scaled errors from 1σ lower and upper limits. When the median counts in a given flux bin are zero, we only list uncertainties from the 16th and 84th percentiles, because we cannot associate an effective area to flux bins that lack information about demagnified peak intensities. These counts are also presented in Figs. 9 and 10, where median counts for individual models in each cluster field are also displayed. Error bars shown in these Figs. combine the uncertainties from the 16th and 84th percentiles in quadrature with those from scaled Poisson confidence levels for 1σ lower and upper limits, respectively. Table 4 details the lens models included for computing the median counts at a given flux density for each cluster field, chosen as those where at least one realization of the Monte Carlo simulation has non-zero counts (see §3.6).

Because of the small number statistics, we expect our detections to give large error bars in the derived number counts. Uncertainties coming from our Monte Carlo simulation (i.e., using the whole probability distributions for observed flux densities, source redshifts and magnifications together) differ by a factor of $\sim 0.02 - 5.5$ from Poisson scatter. In A2744 and MACSJ1149, they dominate the upper error bars in the cumulative counts at flux densities below ~ 0.1 mJy (see Table 3). This arises from the broad magnification distributions found in some of the faintest observed sources in these cluster fields. High magnifications make them the intrinsically faintest sources, with demagnified flux densities below ~ 0.1 mJy and effective areas below 0.1 arcmin^2 (see also Fig. 7). For the faintest source in these cluster fields, the effective area distributions easily reach 0.03 arcmin^2 and below, which in turn elevates the counts at their flux levels. This combination of broad distributions both in demagnified flux and effective area makes the number counts below ~ 0.1 mJy highly uncertain.

We present counts down to the flux density where at least one cluster field has non-zero combined differential counts at the 84th percentile, i.e. centred on 0.007 mJy. Combining all cluster fields, our differential counts eventually span ~ 2.5 orders of magnitude in demagnified flux density, going from the mJy level down to tens of μJy . This is ≈ 4 times deeper than the observed rms level reached by the ALMA FF mosaics.

We find variations across lens models in the median counts per flux bin up to ≈ 1 dex (considering models giving non-zero median differential counts in a flux bin). Despite this, in all clus-

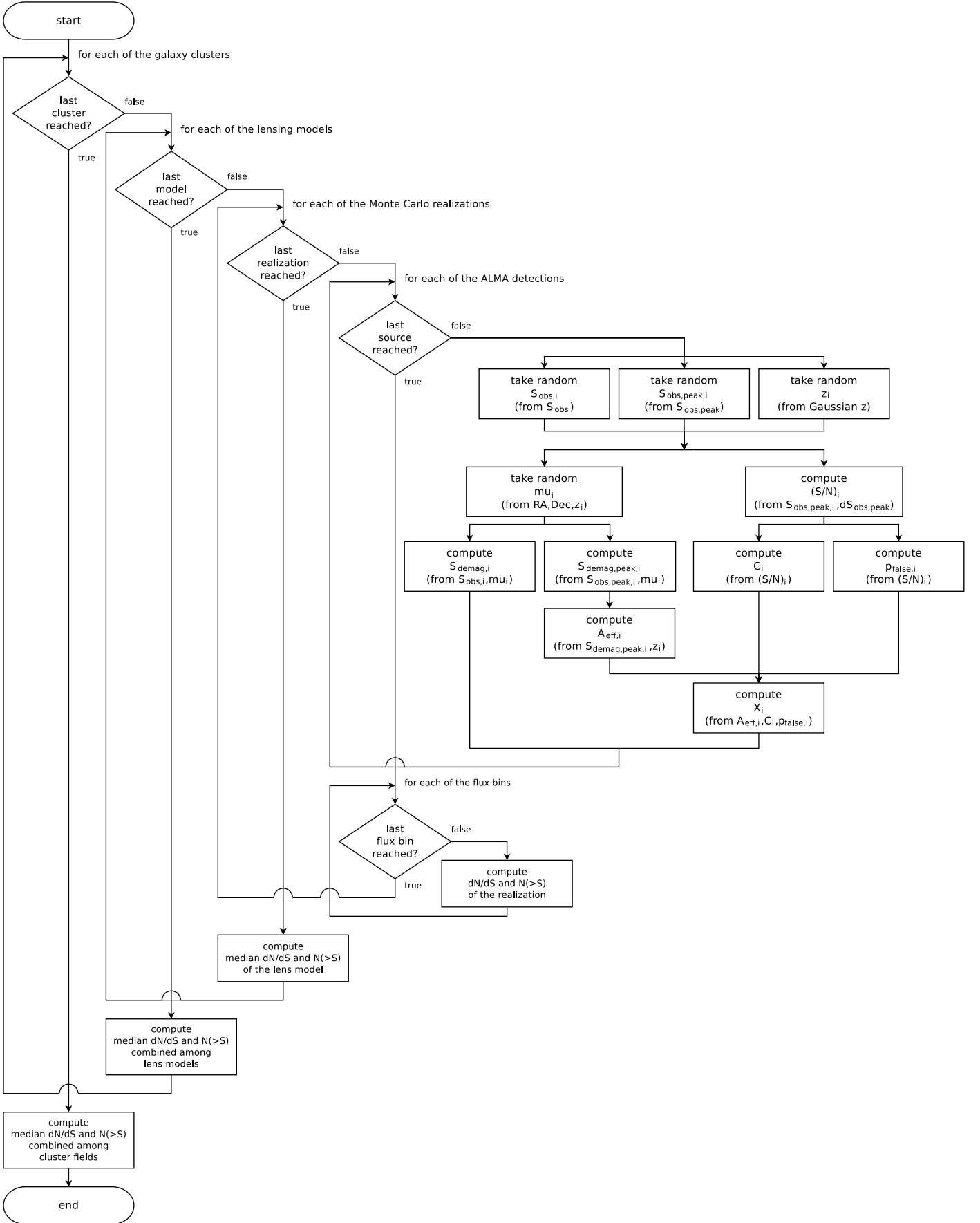


Fig. 8. Diagram of the Monte Carlo simulation developed for estimating demagnified number counts (see details in §3.6).

Table 3. Demagnified 1.1 mm number counts.

Cluster field	$S_{1.1\text{ mm}}$ [mJy]	$dN/d\log(S)$ [deg ⁻²]	# sources	$S_{1.1\text{ mm}}$ [mJy]	$N(> S)$ [deg ⁻²]	# sources
A2744	0.007	$0.000^{+3.346}_{-0.000} \times 10^5$	$0.0^{+1.0}_{-0.0} +1.8$	0.004	$(9.717^{+14.04}_{-7.209} +4.437)$	$9.0^{+1.0}_{-1.0} +4.1$
	0.024	$0.000^{+2.349}_{-0.000} \times 10^5$	$0.0^{+0.0}_{-0.0} +1.8$	0.013	$(7.332^{+7.551}_{-5.128} +3.348)$	$9.0^{+1.0}_{-1.0} +4.1$
	0.075	$(1.503^{+6.343}_{-1.503} +3.457) \times 10^4$	$1.0^{+1.0}_{-0.0} +2.3$	0.042	$(2.446^{+3.143}_{-0.749} +1.208)$	$8.0^{+1.0}_{-1.0} +2.9$
	0.237	$(1.431^{+0.817}_{-0.915} +1.887) \times 10^4$	$1.0^{+1.0}_{-0.0} +2.6$	0.133	$(1.647^{+0.259}_{-0.180} +0.889)$	$7.0^{+1.0}_{-0.0} +2.8$
	0.750	$(1.615^{+0.507}_{-0.764} +1.277) \times 10^4$	$4.0^{+1.0}_{-2.0} +3.3$	0.422	$(9.876^{+2.788}_{-3.121} +8.680)$	$5.0^{+1.0}_{-2.0} +3.4$
	2.371	$(4.367^{+0.241}_{-0.951} +10.64) \times 10^3$	$1.0^{+0.0}_{-0.0} +2.3$	1.334	$(2.183^{+0.475}_{-0.475} +5.057)$	$1.0^{+0.0}_{-0.0} +2.3$
MACSJ0416	0.007	$0.000^{+0.000}_{-0.000}$	$0.0^{+0.0}_{-0.0} +1.8$	0.004	$(1.636^{+0.608}_{-0.568} +1.396)$	$4.0^{+1.0}_{-1.0} +3.2$
	0.024	$0.000^{+0.000}_{-0.000}$	$0.0^{+0.0}_{-0.0} +1.8$	0.013	$(1.636^{+0.608}_{-0.568} +1.396)$	$4.0^{+1.0}_{-1.0} +3.2$
	0.075	$0.000^{+0.000}_{-0.000}$	$0.0^{+0.0}_{-0.0} +1.8$	0.042	$(1.632^{+0.568}_{-0.568} +1.281)$	$4.0^{+1.0}_{-1.0} +3.2$
	0.237	$(2.602^{+1.445}_{-0.675} +2.531) \times 10^4$	$3.0^{+1.0}_{-0.0} +2.9$	0.133	$(1.533^{+0.568}_{-0.568} +0.733)$	$4.0^{+1.0}_{-1.0} +3.2$
	0.750	$(3.934^{+0.548}_{-0.675} +3.254) \times 10^3$	$1.0^{+0.0}_{-0.0} +3.5$	0.422	$(1.967^{+0.337}_{-0.337} +1.677)$	$1.0^{+0.0}_{-0.0} +2.3$
	2.371	$0.000^{+0.000}_{-0.000}$	$0.0^{+0.0}_{-0.0} +1.8$	1.334	$0.000^{+0.000}_{-0.000}$	$0.0^{+0.0}_{-0.0} +0.8$
MACSJ1149	0.007	$0.000^{+0.000}_{-0.000}$	$0.0^{+0.0}_{-0.0} +1.8$	0.004	$(2.525^{+8.121}_{-8.811} +3.330)$	$2.0^{+1.0}_{-1.0} +2.6$
	0.024	$0.000^{+0.000}_{-0.000}$	$0.0^{+0.0}_{-0.0} +1.8$	0.013	$(2.501^{+6.788}_{-6.788} +1.593)$	$2.0^{+1.0}_{-1.0} +2.3$
	0.075	$0.000^{+1.385}_{-0.000} \times 10^5$	$0.0^{+1.0}_{-0.0} +1.8$	0.042	$(1.354^{+0.211}_{-0.113} +1.945)$	$2.0^{+1.0}_{-1.0} +2.3$
	0.237	$(1.539^{+1.206}_{-0.858} +3.539) \times 10^4$	$1.0^{+0.0}_{-0.0} +2.3$	0.133	$(8.561^{+0.113}_{-4.502} +1.873)$	$2.0^{+0.0}_{-1.0} +2.3$
	0.750	$0.000^{+4.515}_{-0.000} \times 10^3$	$0.0^{+1.0}_{-0.0} +1.8$	0.422	$0.000^{+2.257}_{-0.000} \times 10^3$	$0.0^{+1.0}_{-0.0} +1.8$
	2.371	$0.000^{+0.000}_{-0.000}$	$0.0^{+0.0}_{-0.0} +1.8$	1.334	$0.000^{+0.000}_{-0.000}$	$0.0^{+0.0}_{-0.0} +0.8$
Combined	0.007	$0.000^{+0.000}_{-0.000}$	$0.0^{+0.0}_{-0.0} +1.8$	0.004	$(2.309^{+10.11}_{-7.232} +1.826)$	$4.0^{+3.0}_{-3.0} +3.2$
	0.024	$0.000^{+1.224}_{-0.000} \times 10^5$	$0.0^{+1.0}_{-0.0} +1.8$	0.013	$(2.225^{+7.888}_{-3.132} +1.759)$	$4.0^{+3.0}_{-3.0} +3.2$
	0.075	$0.000^{+6.889}_{-0.000} \times 10^4$	$0.0^{+1.0}_{-0.0} +1.8$	0.042	$(1.902^{+2.826}_{-0.921} +1.905)$	$4.0^{+4.0}_{-3.0} +3.2$
	0.237	$(1.818^{+1.373}_{-0.978} +2.398) \times 10^4$	$2.0^{+2.0}_{-0.0} +2.6$	0.133	$(1.487^{+0.460}_{-0.249} +1.176)$	$4.0^{+3.0}_{-2.0} +3.2$
	0.750	$(4.073^{+12.28}_{-4.973} +3.367) \times 10^3$	$1.0^{+3.0}_{-1.0} +2.3$	0.422	$(2.041^{+0.789}_{-2.041} +4.694)$	$1.0^{+2.0}_{-1.0} +2.3$
	2.371	$(4.254^{+0.348}_{-4.254} +3.518) \times 10^3$	$1.0^{+0.0}_{-1.0} +2.3$	1.334	$(2.127^{+0.174}_{-2.127} +1.888)$	$1.0^{+0.0}_{-1.0} +2.3$

Notes. Column 1: cluster field where the counts are computed. In the bottom row group, counts combining all cluster fields are listed. Column 2: flux density bin for differential counts. Column 3: median differential counts per flux bin. For non-zero median counts, uncertainties are given separately using the 16th (84th) percentiles and scaled Poisson confidence levels for 1σ lower (upper) limits. For zero median counts, only uncertainties using the 16th and 84th percentiles are provided. Column 4: median number of sources per flux bin. Uncertainties are given separately using the 16th (84th) percentiles and Poisson confidence levels for 1σ lower (upper) limits. Column 5: flux density limit for cumulative counts. Column 6: median cumulative counts per flux limit. Uncertainties are as in Column 3. Column 7: median number of sources per flux limit. Uncertainties are as in Column 4.

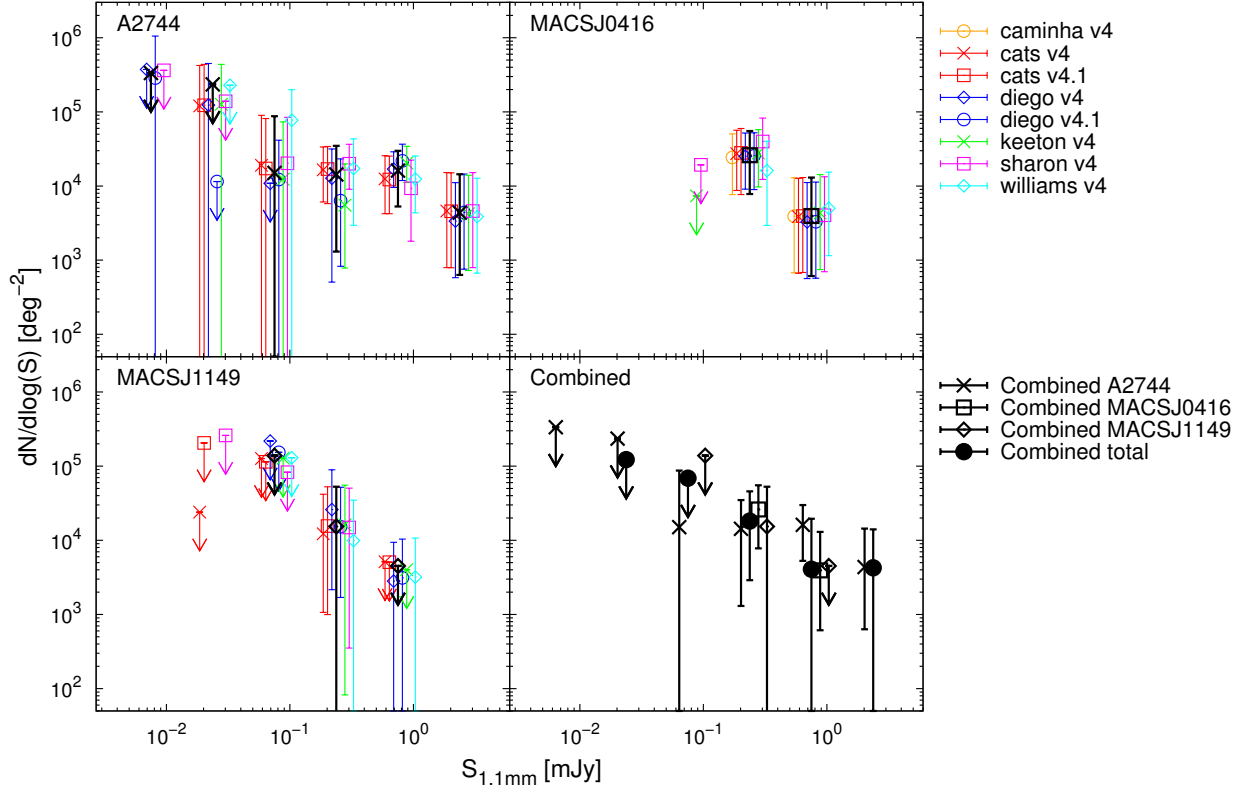


Fig. 9. Demagnified differential counts at 1.1 mm, for each cluster (see legends at top-left) and combining all cluster fields (bottom-right panel). Values correspond to median counts for the lens models listed in Table 2 (colored symbols), combining all models for each cluster field (large black crosses, squares and diamonds) and combining all models for all cluster fields (large black filled circles). Error bars indicate the 16th and 84th percentiles, adding the scaled Poisson confidence levels for 1σ lower and upper limits respectively in quadrature. Upper limits indicate the 84th percentiles for flux density bins having zero median counts. In the first three panels, counts for each model have been offset in flux around the combined counts for clarity. In the bottom-right panel, this is done for each galaxy cluster field around the counts that combine all models for all cluster fields.

ter fields the median counts given by each model per flux bin are consistent within the error bars. A rough agreement among lens models was also found by Coe et al. (2015) when using models (at that time based on pre-FF data only) for predicting the $z > 6$ NIR number counts in all the FFs. They found consistency among all models on the number of faint (i.e. at the nJy level) NIR-detected galaxies expected in HST FF observations.

We explored the effect of adopting different source redshifts in the predicted counts. Within the uncertainties, our differential counts combining all cluster fields and using redshift probability distributions according to available data (as above) are consistent with those obtained assuming a Gaussian redshift distribution centred at $z = 2 \pm 0.5$ for all detections. We also obtain consistent results adopting exactly $z = 2$ for all detections, as well as when assuming a uniform redshift distribution between the cluster redshift and 4. In these three cases, variations in the median counts combining all cluster fields are only up to ≈ 0.04 dex below 1.3 mJy. Our combined counts are also in agreement within the errors with those obtained centring the Gaussian at $z = 3 \pm 0.5$ for all detections (although upper error bars assuming this higher redshift center are greater by ≈ 0.25 dex at $\lesssim 0.1$ mJy, due to the larger high-magnification regions for this redshift).

4.2. Comparison to previous ALMA studies

Fig. 11 shows our 1.1 mm number counts compared to results from recent ALMA observations that probe down to the sub-

mJy level. These include counts derived from sources detected by serendipitous (Ono et al. 2014; Carniani et al. 2015; Fujimoto et al. 2016; Oteo et al. 2016) as well as dedicated surveys in blank fields (Hatsukade et al. 2016; Aravena et al. 2016; Dunlop et al. 2017) and around a $z = 3.09$ protocluster (Umehata et al. 2017). It should be noted that these previous works use their own source detection criterion, as well as their own choice and methodology for computing corrections to the counts (e.g., completeness, flux deboosting, probability of a false detection, effective areas, magnifications). Recalculating their counts matching our criteria, which would ensure a fair comparison, is beyond the scope of this work. Instead, we only apply a scaling for previous counts derived at wavelengths other than 1.1 mm. In those cases, we scale their estimates as $S_{1.1\text{ mm}} = 1.29 \times S_{1.2\text{ mm}}$ and $S_{1.1\text{ mm}} = 1.48 \times S_{1.3\text{ mm}}$. These conversion factors are derived by assuming a characteristic modified blackbody spectrum (following Hatsukade et al. 2016), and are adopted for consistency with previous works (which assume distinct SED templates).

Within the uncertainties, our estimates for both differential and cumulative number counts are in good agreement with all the aforementioned works for the $\sim 2 - 3$ brightest bins, i.e. down to 0.422 mJy. At 0.133 – 0.422 mJy, our number counts are consistent within 1σ with all but Fujimoto et al. (2016) and Hatsukade et al. (2016) data. At flux densities fainter than 0.133 mJy, the derived 1σ upper limits to our differential counts are lower than Fujimoto et al. (2016) data by ≈ 0.5 dex, being also inconsistent with their Schechter (1976) best-fitting function by more

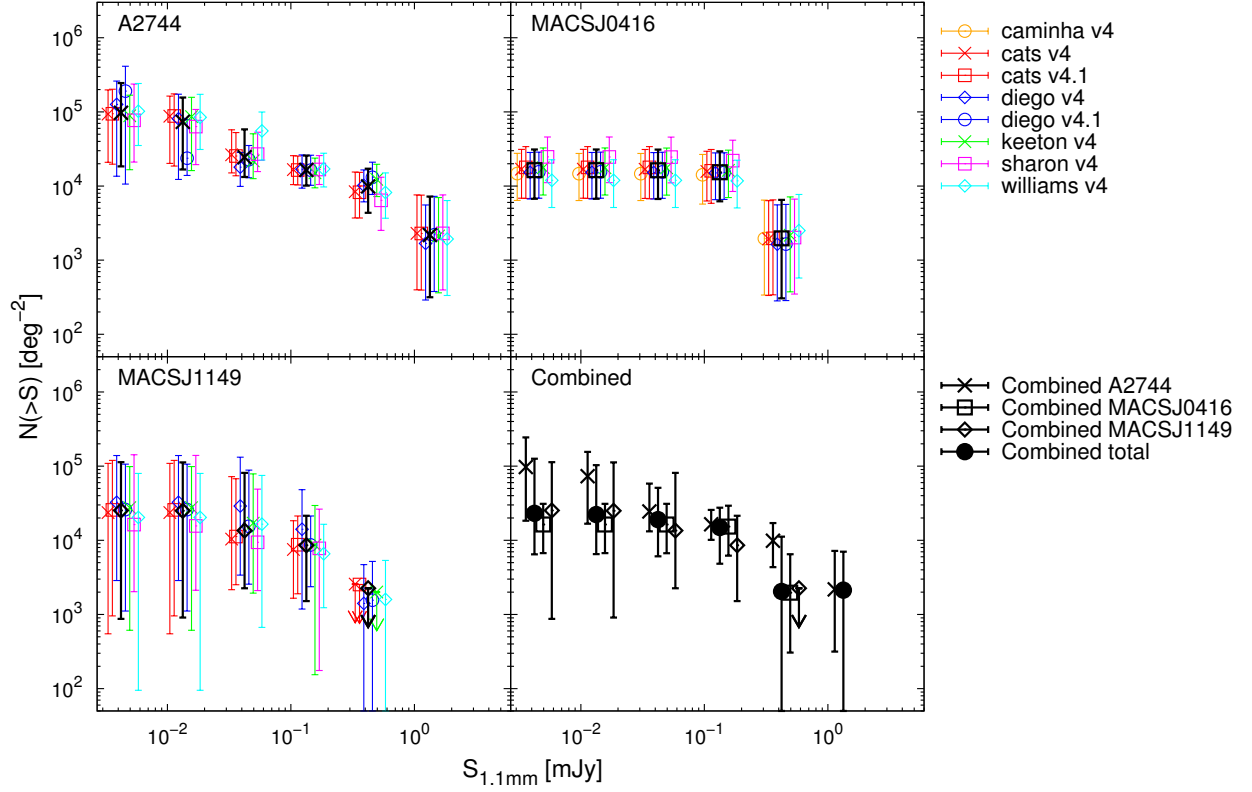


Fig. 10. As in Fig. 9, but for the demagnified cumulative number counts at 1.1 mm.

Table 4. Lensing models considered for computing the median demagnified 1.1 mm number counts at each flux density (see Table 3 and Figs. 9 and 10).

	$S_{1.1\text{ mm}}$ [mJy]	List of models
Differential counts	0.007	A2744: ^{b,c,d,e,f,g,h} ; MACSJ0416: ^{a,b,e,f,g,h} ; MACSJ1149: ^g
	0.024	A2744: ^{b,c,d,e,f,g,h} ; MACSJ0416: ^{a,b,c,d,e,f,g,h} ; MACSJ1149: ^{b,c,d,e,f,g,h}
	0.075	A2744: ^{b,c,d,e,f,g,h} ; MACSJ0416: ^{a,b,c,d,e,f,g,h} ; MACSJ1149: ^{b,c,d,e,f,g,h}
	0.237	A2744: ^{b,c,d,e,f,g,h} ; MACSJ0416: ^{a,b,c,d,e,f,g,h} ; MACSJ1149: ^{b,c,d,e,f,g,h}
	0.750	A2744: ^{b,c,d,e,f,g,h} ; MACSJ0416: ^{a,b,c,d,e,f,g,h} ; MACSJ1149: ^{b,c,d,e,f,g,h}
	2.371	A2744: ^{b,c,d,e,f,g,h} ; MACSJ0416: ^h ; MACSJ1149: -
Cumulative counts	0.004	A2744: ^{b,c,d,e,f,g,h} ; MACSJ0416: ^{a,b,c,d,e,f,g,h} ; MACSJ1149: ^{b,c,d,e,f,g,h}
	0.013	A2744: ^{b,c,d,e,f,g,h} ; MACSJ0416: ^{a,b,c,d,e,f,g,h} ; MACSJ1149: ^{b,c,d,e,f,g,h}
	0.042	A2744: ^{b,c,d,e,f,g,h} ; MACSJ0416: ^{a,b,c,d,e,f,g,h} ; MACSJ1149: ^{b,c,d,e,f,g,h}
	0.133	A2744: ^{b,c,d,e,f,g,h} ; MACSJ0416: ^{a,b,c,d,e,f,g,h} ; MACSJ1149: ^{b,c,d,e,f,g,h}
	0.422	A2744: ^{b,c,d,e,f,g,h} ; MACSJ0416: ^{a,b,c,d,e,f,g,h} ; MACSJ1149: ^{b,c,d,e,f,g,h}
	1.334	A2744: ^{b,c,d,e,f,g,h} ; MACSJ0416: ^h ; MACSJ1149: -

Notes. Column 1: type of number counts. Column 2: flux density bin (limit) for differential (cumulative) counts. Column 3: lens models found to have at least one Monte Carlo realization (out of 1000) having non-zero counts at this flux. Lens models: ^(a) Caminha v4; ^(b) CATS v4; ^(c) CATS v4.1; ^(d) Diego v4; ^(e) Diego v4.1; ^(f) Keeton v4; ^(g) Sharon v4; ^(h) Williams v4.

than 2σ . Also below this flux density, our cumulative counts are lower by ≈ 1 dex than Aravena et al. (2016) data, being inconsistent with their results at a 3σ level. These findings suggest a flattening of the number counts.

The counts derived from serendipitously detected sources are based on detections in fields that targeted a previously defined set of sources. These counts are expected to be biased, as the detections might be clustered around the original targets (Hatsukade et al. 2016). Restricting only to flux densities above 0.133 mJy,

we are not able to quantify this bias, given the large uncertainties in our derived counts. Neither can we make a strong distinction between our counts, which are based solely on observations lensed by galaxy clusters, and those derived from blank-field observations. Intriguingly, our counts in the brighter flux density bins are consistent with those found by Umehata et al. (2017) toward the SSA22 protocluster, both including and not including their detections having spectroscopic redshifts coincident with the protocluster (in Fig. 11 we show only the first case).

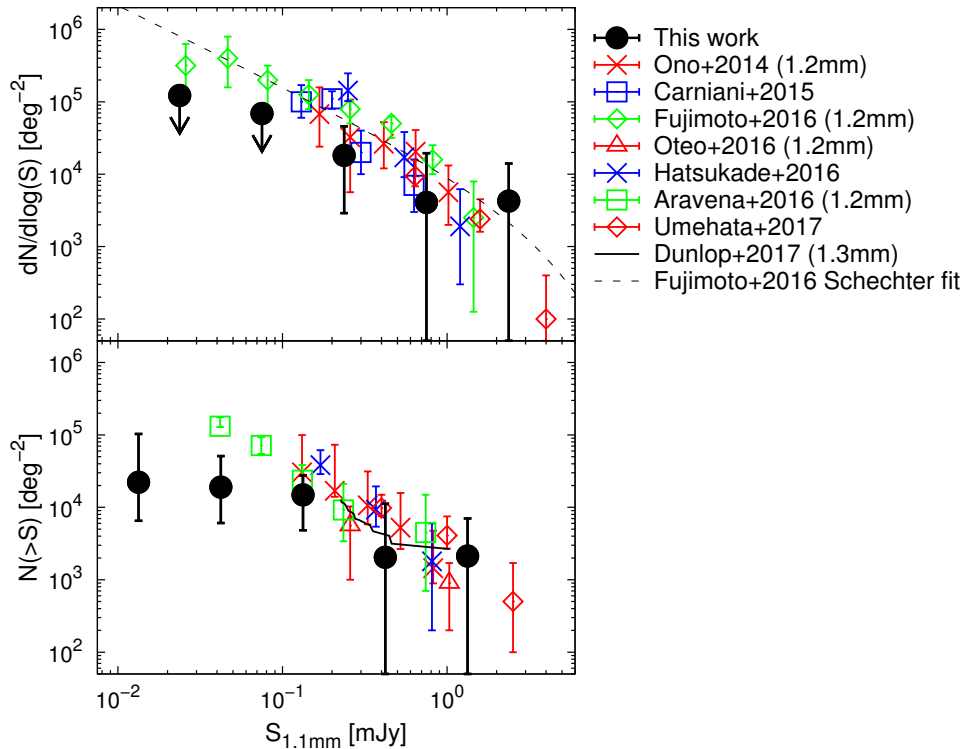


Fig. 11. Differential (top) and cumulative (bottom) counts at 1.1 mm compared to ALMA results from the literature. Our counts (large black filled circles) correspond to median values combining all models for all cluster fields. Error bars indicate the 16th and 84th percentiles, adding the scaled Poisson confidence levels for 1σ lower and upper limits respectively in quadrature. The upper limits indicate the 84th percentile for flux density bins having zero median counts. We show previous results reported by Ono et al. (2014) as red crosses, Carniani et al. (2015) as blue squares, Fujimoto et al. (2016) as green diamonds (with their Schechter fit shown as a black dashed line), Oteo et al. (2016) as red triangles, Hatsukade et al. (2016) as blue crosses, Aravena et al. (2016) as green squares, Umehata et al. (2017) as red diamonds and Dunlop et al. (2017) as a black solid curve. We scale the counts derived at other wavelengths as $S_{1.1\text{mm}} = 1.29 \times S_{1.2\text{mm}}$ and $S_{1.1\text{mm}} = 1.48 \times S_{1.3\text{mm}}$ (following Hatsukade et al. 2016).

Below 0.133 mJy, our number counts are inconsistent with available data from both serendipitous and blank-field surveys. This discrepancy could be attributed to cosmic variance or to the aforementioned observational biases. However, it may also reveal the need for further corrections in our number counts. More specifically, we may require a proper treatment for the stretching that source shapes experience in the image plane (see §3.1). Accounting for this could elevate the derived number counts in the faint end, if the dust emission from low-significance detections is more extended than suggested by extrapolations to current observational data (Fujimoto et al. 2017 and González-López et al. 2018 in prep., see §2.1.2). We leave a detailed analysis about the impact of source geometries on the number counts for future work.

We use the Monte Carlo realizations of the differential number counts to compute the contribution to the EBL provided by each of them, adding up the contribution contained in each flux bin. From this procedure, we estimate a median contribution of $6.055^{+7.969}_{-2.836}$ ($3.315^{+8.028}_{-1.785}$) Jy deg^{-2} resolved in our demagnified sources at 1.1 mm down to 0.013 (0.133) mJy, with uncertainties computed from the 16th and 84th percentiles.

We compare our estimate with the total EBL measurement at that wavelength measured by the Planck collaboration. Following Aravena et al. (2016), we interpolate the Planck measurements (see Planck Collaboration et al. 2014, Table 10) finding an EBL of $19.143^{+0.751}_{-0.723}$ Jy deg^{-2} at 263.14 GHz, which is the set Local Oscillator frequency for our observations (see Paper I). The contribution provided by our demagnified sources rep-

resents $32^{+42}_{-15}\%$ ($17^{+42}_{-9}\%$) of this EBL at 1.1 mm down to 0.013 (0.133) mJy. As expected from Fig. 11, this contribution is lower than (although consistent to $\approx 1.5\sigma$ with) results by Carniani et al. (2015) and Hatsukade et al. (2016), both at 1.1 mm. Carniani et al. (2015) found an estimate of 17^{+10}_{-5} Jy deg^{-2} down to 0.1 mJy, while a value around 12 (14) Jy deg^{-2} is obtained when we extrapolate the Schechter (double power law) best-fitting function by Hatsukade et al. (2016) down to 0.1 mJy.

5. Summary

We have derived lensing-corrected number counts at 1.1 mm exploiting 1) the high resolution and depth reached in a dedicated ALMA survey of three galaxy clusters (i.e., A2744, MACSJ0416 and MACSJ1149) as part of the Frontier Fields program, and 2) the public availability of several models for the mass reconstruction of these clusters. This is the first time that the surface density of DSFGs is estimated around three well-studied galaxy clusters using ALMA data. Our source catalog includes $S/N \geq 5$ detections already introduced with the ALMA Frontier Fields Survey (Paper I), plus $4.5 \leq S/N < 5$ detections reported in the present work. We correct the counts for completeness and probability of false detection. Moreover, we develop a careful treatment to fold the magnification uncertainties in the derived counts using a Monte Carlo simulation.

Our ALMA mosaics of the three FF galaxy clusters cover a total observed area of $\sim 14 \text{ arcmin}^2$, which results in a smaller effective area in the source plane once a lens model is applied

(e.g. the total area is reduced by ~ 2.6 times in the CATS v4 model for a source-plane $z = 2$). Combining all cluster fields, our differential number counts span ~ 2.5 orders of magnitude in demagnified flux density, going from the mJy level down to tens of μ Jy. We find an overall agreement between the counts derived for different lens models in a given cluster field. Within the error bars in our number counts (coming from both Poisson errors and lensing model uncertainties) our results are consistent with recent estimates from deep ALMA observations (Ono et al. 2014; Carniani et al. 2015; Fujimoto et al. 2016; Oteo et al. 2016; Hatsukade et al. 2016; Aravena et al. 2016; Umehata et al. 2017; Dunlop et al. 2017) only down to ≈ 0.1 mJy. At fainter flux densities, both our differential and cumulative number counts are inconsistent with previous estimates, being lower by ≈ 0.5 and ≈ 1 dex, respectively. This suggests a flattening of the number counts, and implies that we may finally be seeing a turn over. Future work including further FFs (González-López et al. 2018b, in prep.; Muñoz Arancibia et al. 2018, in prep.) should help to reduce the uncertainties in these results.

Since our detection criterion is based solely on the source peak S/N, we do not add constraints on the angular size of the sources. However, it should be noted that there may be extended sources in the image plane having the same integrated flux as the sources found, but were not detected since they do not have a peak S/N ≥ 4.5 . In addition, there may be sources missed because their high magnifications led them to have lensed angular sizes greater than a synthesized beam. In order to take these effects into account, we would need to assume a distribution of source sizes at several redshifts and a set of different source geometries, as well as passing them through the uv and lens modeling. This is beyond the scope of this work, so at low flux densities our reported counts are strictly computed for the beam size quoted for each ALMA mosaic.

Using publicly available lens models, we are able to derive 1.1 mm number counts around three galaxy clusters down to ≈ 4 times deeper than the rms level reached by the ALMA mosaics that target them. This highlights the potential of finding even fainter sources in these FFs with deeper ALMA data, suggesting that future 1.1 mm observations reaching an rms of 10μ Jy could yield number counts down to $\approx 2.5 \mu$ Jy in these fields. Additionally, further spectroscopic redshift determinations for our detections could serve as new constraints for lensing models, helping to increase the accuracy in the magnification estimates (Johnson & Sharon 2016) and hence in the number counts derived from future deep surveys.

Acknowledgements. We acknowledge support from CONICYT through FONDECYT grant 3160776 (A.M.M.A.), CONICYT grants BASAL-CATA PFB-06/2007 (F.E.B.), FONDECYT Regular 1141218 (F.E.B., J.G.-L.), Programa de Cooperación Científica ECOS-CONICYT C16U02 (F.E.B., J.G.-L.), Programa de Astronomía FONDO ALMA 2016 31160033 (J.G.-L.), the Ministry of Economy, Development, and Tourism's Millennium Science Initiative through grant IC120009, awarded to The Millennium Institute of Astrophysics, MAS, Chile (C.R.-C. and F.E.B.) and CONICYT through FONDECYT grant 3150238 (C.R.-C.). E.I. acknowledges partial support from FONDECYT through grant 1171710. R.D. gratefully acknowledges the support provided by the BASAL Center for Astrophysics and Associated Technologies (CATA). The ALMA observations were carried out under program ADS/JAO.ALMA#2013.1.00999.S. ALMA is a partnership of ESO (representing its member states), NSF (USA) and NINS (Japan), together with NRC (Canada) and NSC and ASIAA (Taiwan), in cooperation with the Republic of Chile. The Joint ALMA Observatory is operated by ESO, AUI/NRAO and NAOJ. This work utilizes gravitational lensing models produced by PIs Bradač, Natarajan & Kneib (CATS), Merten & Zitrin, Sharon, Williams, Keeton, Bernstein and Diego, and the GLAFIC group. This lens modeling was partially funded by the HST Frontier Fields program conducted by STScI. STScI is operated by the Association of Universities for Research in Astronomy, Inc. under NASA contract NAS 5-26555. The lens models were obtained from the Mikulski Archive for Space Telescopes (MAST).

References

- Acebron, A., Jullo, E., Limousin, M., et al. 2017, *MNRAS*, 470, 1809
 Ammons, S. M., Wong, K. C., Zabludoff, A. I., & Keeton, C. R. 2014, *ApJ*, 781, 2
 Aravena, M., Decarli, R., Walter, F., et al. 2016, *ApJ*, 833, 68
 Balestra, I., Mercurio, A., Sartoris, B., et al. 2016, *ApJS*, 224, 33
 Béthermin, M., De Breuck, C., Sargent, M., & Daddi, E. 2015, *A&A*, 576, L9
 Blain, A. W., Kneib, J.-P., Ivison, R. J., & Smail, I. 1999, *ApJ*, 512, L87
 Blain, A. W., Smail, I., Ivison, R. J., Kneib, J.-P., & Frayer, D. T. 2002, *Phys. Rep.*, 369, 111
 Bouwens, R. J., Oesch, P. A., Illingworth, G. D., Ellis, R. S., & Stefanon, M. 2017, *ApJ*, 843, 129
 Busmann, S., Leung, T. K., & Conley, A. 2016, *uvmmcf: Parametric models to interferometric data fitter*, *Astrophysics Source Code Library*
 Caminha, G. B., Grillo, C., Rosati, P., et al. 2017, *A&A*, 600, A90
 Carniani, S., Maiolino, R., De Zotti, G., et al. 2015, *A&A*, 584, A78
 Casey, C. M., Narayanan, D., & Cooray, A. 2014, *Phys. Rep.*, 541, 45
 Castellano, M., Amorín, R., Merlin, E., et al. 2016, *A&A*, 590, A31
 Chapman, S. C., Blain, A. W., Smail, I., & Ivison, R. J. 2005, *ApJ*, 622, 772
 Coe, D., Bradley, L., & Zitrin, A. 2015, *ApJ*, 800, 84
 Coe, D., Fuselier, E., Benítez, N., et al. 2008, *ApJ*, 681, 814
 Coppin, K., Chapin, E. L., Mortier, A. M. J., et al. 2006, *MNRAS*, 372, 1621
 Di Criscienzo, M., Merlin, E., Castellano, M., et al. 2017, *A&A*, 607, A30
 Diego, J. M., Broadhurst, T., Molnar, S. M., Lam, D., & Lim, J. 2015, *MNRAS*, 447, 3130
 Diego, J. M., Protopapas, P., Sandvik, H. B., & Tegmark, M. 2005, *MNRAS*, 360, 477
 Diego, J. M., Tegmark, M., Protopapas, P., & Sandvik, H. B. 2007, *MNRAS*, 375, 958
 Dunlop, J. S., McLure, R. J., Biggs, A. D., et al. 2017, *MNRAS*, 466, 861
 Ebeling, H., Ma, C.-J., & Barrett, E. 2014, *ApJS*, 211, 21
 Fujimoto, S., Ouchi, M., Ono, Y., et al. 2016, *ApJS*, 222, 1
 Fujimoto, S., Ouchi, M., Shibuya, T., & Nagai, H. 2017, *ApJ*, 850, 83
 Gehrels, N. 1986, *ApJ*, 303, 336
 González-López, J., Bauer, F. E., Romero-Cañizales, C., et al. 2017, *A&A*, 597, A41
 Greve, T. R., Bertoldi, F., Smail, I., et al. 2005, *MNRAS*, 359, 1165
 Grillo, C., Karman, W., Suyu, S. H., et al. 2016, *ApJ*, 822, 78
 Hatsukade, B., Kohno, K., Umehata, H., et al. 2016, *PASJ*, 68, 36
 Hezaveh, Y. D. & Holder, G. P. 2011, *ApJ*, 734, 52
 Hoag, A., Huang, K.-H., Treu, T., et al. 2016, *ApJ*, 831, 182
 Hodge, J. A., Karim, A., Smail, I., et al. 2013, *ApJ*, 768, 91
 Hogg, D. W. & Turner, E. L. 1998, *PASP*, 110, 727
 Hsu, L.-Y., Cowie, L. L., Chen, C.-C., Barger, A. J., & Wang, W.-H. 2016, *ApJ*, 829, 25
 Hughes, D. H., Serjeant, S., Dunlop, J., et al. 1998, *Nature*, 394, 241
 Jauzac, M., Clément, B., Limousin, M., et al. 2014, *MNRAS*, 443, 1549
 Jauzac, M., Richard, J., Jullo, E., et al. 2015, *MNRAS*, 452, 1437
 Jauzac, M., Richard, J., Limousin, M., et al. 2016, *MNRAS*, 457, 2029
 Johansson, D., Sigurdsson, H., & Horellou, C. 2011, *A&A*, 527, A117
 Johnson, T. L. & Sharon, K. 2016, *ApJ*, 832, 82
 Johnson, T. L., Sharon, K., Bayliss, M. B., et al. 2014, *ApJ*, 797, 48
 Jullo, E. & Kneib, J.-P. 2009, *MNRAS*, 395, 1319
 Jullo, E., Kneib, J.-P., Limousin, M., et al. 2007, *New Journal of Physics*, 9, 447
 Karim, A., Swinbank, A. M., Hodge, J. A., et al. 2013, *MNRAS*, 432, 2
 Kawamata, R., Oguri, M., Ishigaki, M., Shimasaku, K., & Ouchi, M. 2016, *ApJ*, 819, 114
 Keeton, C. R. 2010, *General Relativity and Gravitation*, 42, 2151
 Kneib, J.-P. & Natarajan, P. 2011, *A&A Rev.*, 19, 47
 Knudsen, K. K., van der Werf, P. P., & Kneib, J.-P. 2008, *MNRAS*, 384, 1611
 Laporte, N., Bauer, F. E., Trancoso-Iribarren, P., et al. 2017, *A&A*, 604, A132
 Liesenborgs, J., De Rijcke, S., & Dejonghe, H. 2006, *MNRAS*, 367, 1209
 Liesenborgs, J., de Rijcke, S., Dejonghe, H., & Bekaert, P. 2007, *MNRAS*, 380, 1729
 Lotz, J. M., Koekemoer, A., Coe, D., et al. 2017, *ApJ*, 837, 97
 Mahler, G., Richard, J., Clément, B., et al. 2018, *MNRAS*, 473, 663
 McCully, C., Keeton, C. R., Wong, K. C., & Zabludoff, A. I. 2014, *MNRAS*, 443, 3631
 Meneghetti, M., Natarajan, P., Coe, D., et al. 2017, *MNRAS*, 472, 3177
 Molino, A., Benítez, N., Ascaso, B., et al. 2017, *MNRAS*, 470, 95
 Ono, Y., Ouchi, M., Kurono, Y., & Momose, R. 2014, *ApJ*, 795, 5
 Oteo, I., Zwaan, M. A., Ivison, R. J., Smail, I., & Biggs, A. D. 2016, *ApJ*, 822, 36
 Owers, M. S., Randall, S. W., Nulsen, P. E. J., et al. 2011, *ApJ*, 728, 27
 Pedregosa, F., Varoquaux, G., Gramfort, A., et al. 2012, *ArXiv e-prints* [arXiv:1201.0490]
 Planck Collaboration, Ade, P. A. R., Aghanim, N., et al. 2014, *A&A*, 571, A30
 Pope, A., Scott, D., Dickinson, M., et al. 2006, *MNRAS*, 370, 1185
 Postman, M., Coe, D., Benítez, N., et al. 2012, *ApJS*, 199, 25

- Priewe, J., Williams, L. L. R., Liesenborgs, J., Coe, D., & Rodney, S. A. 2017, MNRAS, 465, 1030
- Rawle, T. D., Altieri, B., Egami, E., et al. 2016, MNRAS, 459, 1626
- Richard, J., Jauzac, M., Limousin, M., et al. 2014, MNRAS, 444, 268
- Safarzadeh, M., Hayward, C. C., Ferguson, H. C., & Somerville, R. S. 2016, ApJ, 818, 62
- Schechter, P. 1976, ApJ, 203, 297
- Sebesta, K., Williams, L. L. R., Mohammed, I., Saha, P., & Liesenborgs, J. 2016, MNRAS, 461, 2126
- Smail, I., Ivison, R. J., & Blain, A. W. 1997, ApJ, 490, L5
- Smolčić, V., Aravena, M., Navarrete, F., et al. 2012, A&A, 548, A4
- Trenti, M. & Stiavelli, M. 2008, ApJ, 676, 767
- Treu, T., Brammer, G., Diego, J. M., et al. 2016, ApJ, 817, 60
- Treu, T., Schmidt, K. B., Brammer, G. B., et al. 2015, ApJ, 812, 114
- Umeshata, H., Tamura, Y., Kohno, K., et al. 2017, ApJ, 835, 98
- Walter, F., Decarli, R., Aravena, M., et al. 2016, ApJ, 833, 67
- Weiß, A., Kovács, A., Coppin, K., et al. 2009, ApJ, 707, 1201
- Younger, J. D., Fazio, G. G., Huang, J.-S., et al. 2007, ApJ, 671, 1531
- Zemcov, M., Blain, A., Halpern, M., & Levenson, L. 2010, ApJ, 721, 424
- Zitrin, A., Fabris, A., Merten, J., et al. 2015, ApJ, 801, 44